The Pennsylvania State University

The Graduate School

PLANAR DEFECTS IN WURTZITE MATERIALS

A Dissertation in

Physics

by

Mohamed Mauroof F. Umar

Submitted in Partial Fulfillment

of the Requirements

for the Degree of

Doctor of Philosophy

December 2022

The dissertation of Mohamed Mauroof F. Umar was reviewed and approved by the following:

Jorge O. Sofo

Professor of Physics and Materials Science & Engineering

Dissertation Advisor

Chair of Committee

Vincent H. Crespi

Professor of Physics, Chemistry, and Materials Science & Engineering

Mauricio Terrones

Verne M. Willaman Professor of Physics

Professor of Chemistry and Materials Science & Engineering

Ismaila Dabo

Professor of Materials Science & Engineering

Nitin Samarth

Professor of Physics

George A. and Margaret M. Downsbrough Department Head

Abstract

The technological importance of Gallium Nitride (GaN), and other wide band-gap semiconductors, for use in optoelectronic and high power transistor electronic devices is indisputable. Wurtzite semiconductor samples are typically grown heteroepitaxially, which often results in a large density of extended defects in samples, stemming from the significant epilayer-substrate lattice mismatches. Understanding the morphologies, electronic characteristics, and formation mechanisms of these defects attract considerable research interest. Such studies, amongst other aspects, provide useful insight toward defect engineering, to inhibit formation deleterious defects and promote formation of beneficial defects.

Inversion domain boundaries (IDB) in wurtzite GaN are an excellent example of an extended defect with beneficial characteristics, for example, exhibiting enhanced emission useful for optoelectronic applications. In this dissertation we present two new models for the atomic structure of inversion domain boundaries. Conventionally, the existing models for IDBs, Holt-IDB and IDB*, are distinguished based on the additional $1/2\,\mathbf{c}$ relative shift between the domains in IDB*. We note the $1/2\,\mathbf{c}$ translation of one of the domains in IDB* can be characterized as a misalignment of stacking planes on either side of the defect.

We introduce a defect notation, that specifies the stacking plane and misalignment of an IDB model, capable of denoting existing IDB models. Our defect notation serves as a convenient tool to enumerate all unique possibilities for stacking plane mismatch between the domains of an IDB yielding two new alternatives IDB models. We perform ab initio density functional theory calculations to determine domain wall energies and assess energetic viability of these new models. One of these new models, labelled IDB$'$, is energetically viable and its domain wall energy is lower than Holt-IDB. Even though IDB$'$ has a higher domain wall energy compared to IDB*, we argue that IDB$'$ may be formed in typical growth conditions. We present evidence from existing literature that confirms the existence of IDB$'$, however the defect plane has been misidentified as Holt-IDB. Further, we use our notation to explore possible models for $\{\bar{1}2\bar{1}0\}$-planar IDBs and prismatic stacking faults, and we perform domain wall energy estimations and evaluate the energetic viability of these models.

Table of Contents

List of Figures

List of Tables

Acknowledgments

The list of people, to whom I owe gratitude for having enriched my time as a graduate student, is too numerous to be fully articulated here. Nevertheless, I would be remiss to not specifically mention the names of those who have had the greatest positive influence on me.

Firstly, I would to express my sincere gratitude to my advisor, *Jorge Sofo* for his able guidance during my Ph. D. research. To *Jorge* - in addition to your able support and guidance as an academic advisor, I truly appreciate your patience and kind-hearted nature. I also would like to extend my gratitude to my committee members, *Vincent Crespi*, *Mauricio Terrones*, and *Ismaila Dabo* for their invaluable feedback and guidance towards improving my research.

I consider myself lucky to have made many great friends at Penn State. To *Ssohrab*, *Leonardo*, *Justin*, *Brett*, and many more - thank you for your companionship, advice when needed, and overall kindness. I would also like to thank my family for their continued support over the years. To my parents and siblings - thank you for believing in me and shaping me in to the person that I am. To my babies, *Bilal* and *Hafsa* - both of you are a limitless source of inspiration (and distraction) to me - for that I am grateful. Last but not least, to my wife, *Shaffana* - thank you for being by my side at every step of the way.

Chapter 1

Introduction

1.1 GaN, other III-V semiconductors, and other related compounds: Technological importance and fabrication methods.

The Nobel prize for physics in 2014 was awarded "for the invention of efficient blue light-emitting diodes which has enabled bright and energy-saving white light sources". The prize winners received this prestigious award for their breakthrough efforts in the search for a semiconductor capable of producing blue LED light. The semiconducting material that led to this breakthrough was Gallium nitride (GaN), a wide band-gap semiconductor which exhibits the wurtzite crystal structure.

In addition to possessing a wide band-gap GaN, and other wurtzite semiconductors, exhibit a wide range of desirable characteristics such as: high electron mobility, strong linear and nonlinear optical response, excellent thermal conductivity, and resistance to

harsh environmental conditions [1, 2]. As such, these materials have a wide range of applications in optoelectronics [3–6], high temperature/power electronics [7, 8], photocatalysis [9], quantum computing [10, 11] to name a few. Consequently, Gallium Nitride, other III-V materials, and wurtzitic semiconductors in general have garnered significant research interest in the past few decades.

GaN and other III-V semiconductor based samples are typically fabricated using metal-organic vapor deposition (MOVCD) [12–15] or molecular beam epitaxy (MBE) [16–19]. GaN growth is typically hetero-epitaxial, where a variety of substrates such as, 6H-SiC [20–22], $MgAl_2O_4$ [23], Si (111) [24], GaAs [25], and ZnO (0001) [26] are used. These substrates have non-negligible lattice mismatch resulting in the formation of a variety of defects. In this dissertation, we focus on planar defects existing in prismatic planes that can be characterized with the defect notation we introduce in sec. 2.1. Namely the planar defects considered are, inversion domain boundaries (IDB) and stacking mismatch boundaries (SMB) in the $\{10\bar{1}0\}$ planes, and $\{\bar{1}2\bar{1}0\}$-planar inversion domain boundaries (aIDB) and prismatic stacking faults (PSF) in the $\{\bar{1}2\bar{1}0\}$ planes. Inversion domain boundaries typically originate at the substrate-epilayer interface; the presence of foreign atoms at this interface has been shown form polarity inverted domains with bounding inversion domain boundaries [27, 28]. Additionally, in nanorods, nanowires, and two dimensional wurtzite samples the formation of polarity inverted domains - and consequently forming IDBs - has been shown to be thermodynamically favorable by lowering the electrostatic potential energy [29, 30].

The estimation of formation energies of defects appearing during epitaxial growth provides guidance into the desired process of growth and helps rationalize the resulting morphology. At the same time, the changes induced by the defects on the electronic states of the system can have an impact on the physical characteristics of the wurtzite

samples. Predictions of atomic microstructure of defects and ab initio calculations on such models are useful tools in efforts to estimate formation energies and probe the electronic signature of defects.

Due to their extended nature planar defects have significant impacts on device fabrication processes and device performance. In particular, defects that extend throughout the $\{10\bar{1}0\}$ of GaN epitaxial films have been observed in transmission electron microscopy (TEM) experiments [21, 31, 32]. Further, GaN is found to exhibit excellent luminescence efficiency despite containing a defect density of $\sim 10^{10}$ /cm ^{2}. This defect density is significantly (~ 6 orders of magnitude) higher than the acceptable levels of defect density for efficient optoelectronic emission in GaAs devices [12]. This observation lead to the hypothesis that a majority of the defects present are electronically inert.

The aforementioned $\{10\bar{1}0\}$-planar defects that originate at the substrate and extend throughout the epilayer can possibly be one of two defect categories; stacking mismatch boundaries(SMB) or inversion domain boundaries(IDB). Northrup et al. have shown that a particular inversion domain boundary model referred to as IDB* is the most suitable configuration for the observed defects [33]. Northrup et al. show that IDB* has the lowest domain wall energy out of the possible defects that can explain the $\{10\bar{1}0\}$-planar defects. Additionally Northrup's IDB* is electronically inert, further confirming their assertion that IDB* best explains the microstructure of $\{10\bar{1}0\}$-planar defects. As such, IDBs are an important category of defects in III-V semi-conductors and in related compounds that have the same wurtzite crystal structure.

1.2 Existing models for atomic structure of inversion domain boundaries.

The non-centrosymmetricity of wurtzite crystals results in spontaneous polarization along the [0001] direction [34, 35]. The structure resulting from the interchanging cation sublattice and anion sublattice, is not identical to the original - having polarization in the opposite direction. Conventionally the polarity of a given simple sample is specified as cation-polar (ex. Ga-polar) or anion-polar (ex. N-polar) in reference to the terminating surface during crystal growth (along [0001]). The polarity of wurtzites affect surface and bulk properties [36, 37], electrical and optical properties [38–41], and crystal growth [42, 43].

Inversion domain domain boundaries refer to a plane separating two domains of a sample, where the domains have opposing polarity. In wurtzites IDBs may manifest in many different plane orientations. Conventionally, due to the prevalence of $\{10\bar{1}0\}$-planar IDBs, the moniker 'IDB' usually refers to the $\{10\bar{1}0\}$-planar manifestation. Alternate orientations are referred to by specifying the orientation as a prefix; for example (0001)-planar IDBs. In this dissertation we will adopt this nomenclature; for convenience, we will also use the label aIDB to refer to $\{\bar{1}2\bar{1}0\}$-planar IDBs.

One of the earliest theoretical predictions of the IDBs in polar materials can be found in the work of Aminoff and Broome [44]. An early prediction for the atomic structure of IDBs (alternately referred to as antiphase boundaries) in wurtzites was proposed by Holt [45]. Holt suggests the experimentally distinguishable cation-polar and anion-polar regions of the polar surfaces indicate the presence of antiphase (polarity mismatched) domains. Consequently a plane separating two abutting antiphase domains is referred to

as an antiphase domain boundary (or IDB). For the microstructure of this planar defect, Holt suggests separating a pristine sample of wurtzite into two domains by a $\{10\bar{1}0\}$ plane. Interchanging the cation and anion sub-lattices in one of the domains reverses the polarity, resulting the plane separating the domains being an antiphase boundary. However, the proposed defect model contains energetically unfavorable cation-cation and anion-anion 'wrong bonds' straddling the defect plane, as shown in fig. 2.4(a). Despite the energetic unfavorability of Holt-IDB model, experimental evidence for the existence of this structure can be found in the literature [46, 47]. However, alternative models for IDBs, that avoid 'wrong bonds' are expected to be more prevalent in wurtzite samples.

A model for IDBs, that does not have 'wrong bonds', was proposed in the work of Austerman and Gehman [48]. Wurtzite is a super-lattice comprising of two hexagonal close packed (hcp) sub-lattices, where each (cation and anion) species exclusively occupies one of the hcp sub-lattices. The Austerman IDB model proposes without disrupting the sublattice corresponding to the larger atom. In the case of Beryllium Oxide (BeO), for which Austerman IDB model was initially proposed, the larger atomic species sublattice is the anion or O sublattice. Leaving the O sublattice undisturbed across the interface and reversing the direction of tetrahedral coordination to the Be sublattice in one of the domains results in the polarity reversal. However, early experimental imaging of $\{10\bar{1}0\}$ IDBs [46, 47, 49] indicate the sublattices corresponding to both species are disrupted by the interface. Further, previous works [30] and our calculations indicate the Austerman model is unstable and relaxes to a different structure.

The widely accepted lowest energy configuration for IDBs in wurtzites was proposed by Northrup et al. [33, 50]. The work titled 'Inversion Domain and Stacking Mismatch Boundaries in GaN' [33], describes the model - designated IDB* - as translating one of the domains - of the Holt-IDB structure, by $\mathbf{c}/2$ parallel to the interface. 'Wrong

bonds' between atoms of the same species is avoided by this shift, as shown in fig. 2.4(b). Northrup et al., from ab-initio calculations, show that the domain wall energy of the IDB* model is significantly lower than the Holt-IDB. Additionally Northrup et al. also analyze stacking mismatch boundaries (SMB) which are an alternative possibility for the structure of, previously mentioned, experimentally observed $\{10\bar{1}0\}$-planar defects that extend throughout GaN epilayers. SMBs are defined as an $\{10\bar{1}0\}$ interface between domains that have the same polarity, but mismatch in stacking sequence. However, SMBs have a higher formation energy than IDB* structure. Additionally, SMBs can easily be terminated by stacking faults (SF), where an SF is a (0001) basal plane where the stacking sequence is locally transformed to the sphalerite stacking sequence ($\cdots ABC \cdots$). These findings led to the conclusion that the IDB* structure was the most suitable explanation for the epilayer spanning $\{10\bar{1}0\}$-planar defect observations.

In addition to the thermodynamic preference of IDB*, Northrup et. al found the IDB* structure does not produce states in the bandgap. The electronically inert nature of IDB* and its prevalence explain the observation robust optoelectronic emission from GaN samples despite seemingly having a prohibitively high density of planar defects that may inhibit emission. On the contrary, photoluminescence and cathodoluminescence spectra of GaN samples indicate up to an order of magnitude enhancement of emission by IDBs [27, 51] and basal stacking faults [52]. Ab initio studies attribute the enhanced emission to the tendency of these defects to act as radiative recombination centers owing to the fact that the local electrostatic potential profile traps carriers close to the interface [53]. As such, fabrication of GaN nanorods and nanowires that contain crystalline arrangements of IDBs for optoelectronic applications is an active area of research [54–58].

1.3 Motivation for introducing new models for inversion domain boundaries.

The discussion in preceding paragraph highlights the importance of the study of existing models for IDBs. In the following we present a few examples that suggest the list of IDB models found in existing literature is not exhaustive. This realization motivates our work in identifying alternative models for IDBs. In the process of proposing alternative models for the atomic structure of IDBs we develop a notation - detailed in sec. 2.1 - to characterize IDB models.

An important example that highlights the need to expand the collection of IDB models can be found in a collection of works containing experimental observations of an IDB* defect intersecting an I_1 stacking fault [59–62]. This interaction results in the transformation of the IDB* defect; existing works identify this transformed defect as the Holt-IDB. However, as we will show in sec. 2.4, this interpretation is incorrect. The misidentification can be directly attributed to the authors being unaware of alternative possible models for the misidentified defect.

As mentioned previously, GaN nanorods and nanowires have significant promise in nano-optoelectronic applications. Various imaging studies performed on such nanostructures indicate the presence of polarity inverted domains (ID) in a majority of samples. Notably, the (0001)-planar cross section of an IDs evolves with epigrowth [63–65]. The mechanisms through which the cross section of an ID evolves is not yet fully understood. The discovery of viable, alternative atomic models for IDBs could provide insight towards understanding these mechanisms.

Recent realizations of ferroelectricity in doped wurtzites such as, $Zn_{1-x}Mg_xO$ [66] and $Al_{1-x}Sc_xN$ [67, 68] provide another example of the need to consider all possible atomic configurations of IDBs. Domain wall motion is considered to be crucial for the characteristic hysteresis loop of polarity switching in ferroelectric materials [65]. Here again, understanding the mechanisms that allow for domain wall motion can be facilitated by an expanded knowledge of possible IDB structures.

1.4 Outline of Dissertation

In this dissertation we report the on our discovery of new models for IDBs. The discovery of the newly proposed models is facilitated by a notation schema that we introduce to characterize existing IDB models. Further, our defect notation is used to explore possible models for other wurtzitic planar defect categories such as: stacking mismatch boundaries, $\{\bar{1}2\bar{1}0\}$-planar IDBs, and prismatic stacking faults.

This dissertation is organized as follows. In chap. 2, we report our findings on IDBs in GaN. Here, we introduce a defect notation to characterize existing IDB models and utilize said defect notation to enumerate all other possible IDB models. This analysis leads to the discovery of two new models for IDBs in GaN. One of the new models - which we refer to as IDB′ - is found to be energetically viable. We also discuss existing works that attribute an experimentally observed defect - resulting from the transformation of an IDB* defect with an I_1 stacking fault - as the Holt-IDB model. We contend that our newly proposed IDB′ model is more suitable to describe the aforementioned transformation of the IDB* defect.

In chap. 3, we evaluate energetics of our newly proposed IDB models in other wurtzitic materials. Further, we analyze other types of planar defects, occurring in

prismatic planes of wurtzites, that are amenable to be denoted by our defect notation. The appendix, provides further details on the choice of parameters and other consideration on our ab-initio density functional theory calculations.

Chapter 2

Inversion Domain Boundaries in Wurtzite Gallium Nitride

Introduction

In this chapter we report on our published results [69] on inversion domain boundaries (IDBs) in wurtzite GaN. An IDB is defined as a $\{10\bar{1}0\}$ plane separating two domains of the GaN crystal, where the spontaneous polarization of the abutting domains have opposite directions. This chapter will serve as an introduction to the notation we introduce to conveniently characterize and analyze planar defects. Further we illustrate the utility of the notation in enumerating all possible configurations of defects that can be denoted by the notation. With the aid of the notation we propose two new models for IDBs in GaN, labelled IDB$'$ and IDB$''$. Of these, IDB$'$ is shown to be energetically viable. Further we show that IDB$'$ is more suitable to describe certain experimentally observed defect planes than have been misidentified as Holt-IDB [59–62].

2.1 Wurtzite crystal structure and Notation for planar defects

2.1.1 Wurtzite crystal structure.

Before we enter into the description of the creation of models for defects of interest, we briefly review the wurtzite crystal structure and describe our notation to clearly identify planar defects.

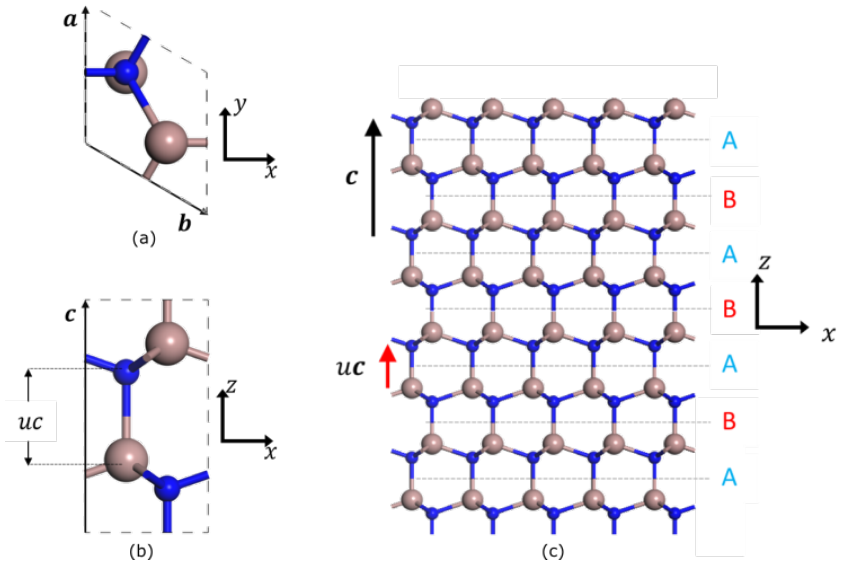

Figure 2.1: (a) (0001)-planar, (b) $(1\bar{2}10)$ views of a wurtzite (GaN) primitive unit cell, and (c) $(1\bar{2}10)$ planar view of Ga-polar GaN sample showing the $\cdots ABAB\cdots$ stacking sequence and $u\mathbf{c}$ vector parallel to $\mathbf{c}$.

The wurtzite crystal structure belongs to the hexagonal crystal system. The primitive unit cell of wurtzite GaN, shown in figure fig. 2.1(a,b), contains a four-atom basis and corresponds to the space group $\mathbf{P6_3mc}$. The lattice parameters obtained by energy minimization are listed in table 2.1 showing a $\frac{c}{a} = 1.629$ which is $\approx 0.2\%$ smaller than the ideal hcp $\frac{c}{a} = \sqrt{\frac{8}{3}}$. The wurtzite structure has a free parameter, $u \approx \frac{3}{8}$, that determines

Table 2.1: Table of calculated lattice parameters of GaN primitive unit cell compared with experimental results.

Lattice Parameter	Calculated	Experimental
a	3.220	3.19 [70]
c	5.246	5.19 [70]
u	0.377	0.377 [71]

the bond length of Ga-N dimers parallel to the c axis.

The wurtzite structure (see fig. 2.1(c)) can be understood as a hexagonal close packed (hcp) lattice with a dimer basis parallel to the **c**-axis. The dimers in the hcp arrangement have an alternating stacking sequence that is denoted by $\cdots ABAB\cdots$. Here A and B refer to the basal plane stacking locations conventionally denoted by A, B and C in hexagonal crystal systems. If the stacking sequences in the two domains of a planar defect are not identical *and* aligned, we say there is a stacking sequence mismatch across the defect plane. Wurtzite being non-centrosymmetric allows for spontaneous polarization which manifests in the [0001] direction [45]. For convenience in identifying the polarity of a domain we assign the vector $u\mathbf{c}$ to be the vector pointing from the Ga atom to the N atom in the the Ga-N dimers bonded parallel to the **c**-axis. By convention, if $u\mathbf{c}$ is parallel to **c** (i.e. $u > 0$), the GaN crystal is referred to as Ga-polar GaN. In the opposite case ($u < 0$) we call it N-polar GaN. We will use the sign of u to differentiate Ga-polar ($u > 0$) from N-polar ($u < 0$) GaN. If the polarity in the two domains of a planar defect are in opposing directions, we say there is a polarity reversal across the defect plane.

2.1.2 Defect Notation for planar defects.

Our notation is motivated by the recognition that existing models for IDBs in wurtzites can be distinguished based stacking sequence mismatch across the IDB defect. Recall the definition of an IDB is, a $\{10\bar{1}0\}$ separating two domains of opposing polarity. There are two existing models for IDBs in the literature: 1) the preferred lowest domain wall energy structure IDB*, proposed by Northrup et al. [33], and 2) Holt-IDB , proposed by Holt [45].

As shown in fig. 2.2(a), the Holt-IDB model refers to a $(10\bar{1}0)$ plane separating two domains, where the Ga and N sublattices are interchanged in one of the domains. The interchange of the species sublattices reverses the direction of the spontaneous polarization, as indicated by the flipping of the direction of the $u\mathbf{c}$ vectors denoted by the red arrows. However, the Holt-IDB model contains Ga-Ga and N-N 'wrong bonds' straddling the defect plane. Due to the energetically unfavorable 'wrong bonds', Holt-IDB has a high domain wall energy. Northup's IDB* model avoids the 'wrong bonds' by introducing a $1/2\,\mathbf{c}$ relative shift between the two domains, as shown in fig. 2.2(b). Bonds across the defect plane IDB* form alternating coplanar-fourfold rings noncoplanar-eightfold rings. Conventionally, the two existing IDB models are distinguished based on

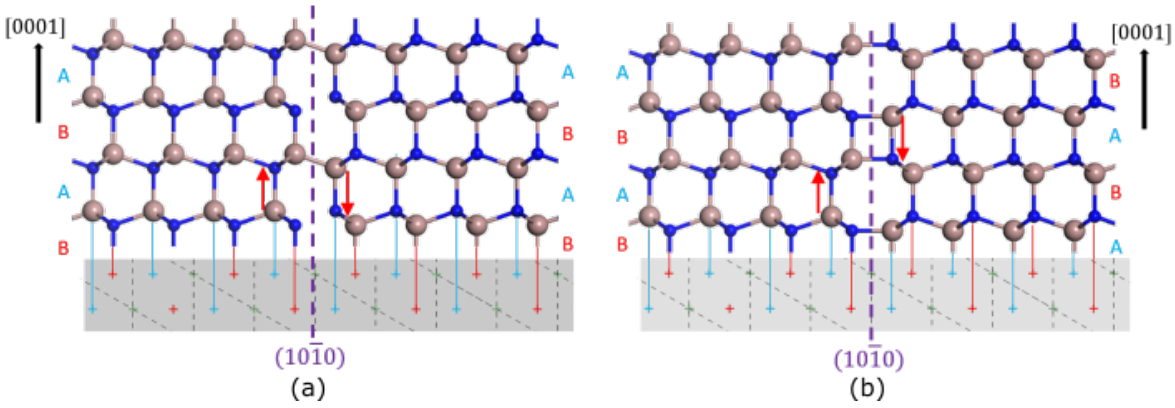

Figure 2.2: $(1\bar{2}10)$ planar views of (a) Holt-IDB, and (b) IDB*.

the 1/2 **c** relative shift between the domains in IDB*. In fig. 2.2 looking at the alignment of stacking planes across the domain wall one notices the stacking planes are aligned in Holt-IDB and misaligned in IDB*.

For example in Holt-IDB, looking at the stacking planes, $A \to A$ and $B \to B$. Additionally, the domains are separated by $\{10\bar{1}0\}$, and the domain on left is Ga-polar ($u > 0$) and the right is N-polar ($u < 0$). The information provided in this paragraph can be succinctly denoted by the notation,

$$\begin{array}{cccc} \cdots & A & B & \cdots_{(+)} \\ \hline \cdots & A & B & \cdots_{(-)} \end{array}_{\{10\bar{1}0\}} . \tag{2.1}$$

. Similarly for IDB*, the stacking plane alignment across the defect plane is $A \to B$ and $B \to A$. Thus IDB* can be denoted by,

$$\begin{array}{cccc} \cdots & A & B & \cdots_{(+)} \\ \hline \cdots & B & A & \cdots_{(-)} \end{array}_{\{10\bar{1}0\}} . \tag{2.2}$$

We can generalize our notation to characterize a multitude of planar defects. The symbol,

$$\begin{array}{cccc} \cdots & \alpha_I & \beta_I & \cdots_{sign(u_I)} \\ \hline \cdots & \alpha_{II} & \beta_{II} & \cdots_{sign(u_{II})} \end{array}_{\{hklm\}}, \tag{2.3}$$

specifies the mismatch in polarity and/or stacking sequence across the $\{hklm\}$ high symmetry plane. For $\{10\bar{1}0\}$-planar IDBs, $\{hklm\} = \{10\bar{1}0\}$. The polarity of each domain is denoted by the $sign(u)$, for example, IDBs will correspond to $u_I \neq u_{II}$. The stacking sequence of domain I is denoted by $\{\alpha_I, \beta_I\}$, each taking values $\{A, B, C\}$ corresponding to the canonical labeling of the stacking in hexagonal lattices. Note that,

for wurtzites the stacking elements are dimers, therefore in each domain α should be different from β to avoid atomic overlap. The ellipses $(\cdots)$ are used to indicate the periodic repetition of stacking planes. The stacking sequence mismatch across the defect plane is read as $\alpha_I \rightarrow \alpha_{II}$ *and* $\beta_I \rightarrow \beta_{II}$.

Note we can simplify our notation, by relabeling stacking plane labels and/or redefining [0001] such that one of the domains has a stacking sequence $\cdots ABAB \cdots$ and has $u > 0$. Hence our notation from (2.3) can be simplified to,

$$\begin{array}{c} \cdots \quad A \quad B \quad \cdots_{(+)} \\ \hline \cdots \quad \alpha \quad \beta \quad \cdots_{sign(u)} \end{array} \cdots \{hklm\}. \tag{2.4}$$

This notation specifies a defect plane by specifying the orientation of the plane ($\{hklm\}$), alignment of polarity (determined by $sign(u)$), and stacking plane alignment across the defect plane (determined by the pair value of (α, β)). With the appropriate choice of $sign(u)$ and $\{hklm\}$, (2.4) can be used to characterize stacking mismatch boundaries, inversion domain boundaries, prismatic stacking faults, and $\{\bar{1}2\bar{1}0\}$-planar inversion domain boundaries. For example, choosing $sign(u)$ as '+' and $\{hklm\} = \{\bar{1}2\bar{1}0\}$, will refer to a prismatic stacking fault.

In our notation there are multiple ways of specifying the same defect due to the periodicity of the stacking sequence and possible permutations of stacking plane labels. Consider the two defect notations,

$$D_1 = \begin{array}{c} \cdots \quad A \quad B \quad \cdots_{(+)} \\ \hline \cdots \quad A \quad C \quad \cdots_{(-)} \end{array} \{10\bar{1}0\}\ , \tag{2.5}$$

and

$$D_2 = \begin{array}{l} \cdots \quad B \quad A \quad \cdots_{(+)} \\ \hline \cdots \quad C \quad A \quad \cdots_{(-)} \end{array}_{\{10\bar{1}0\}} . \tag{2.6}$$

Both defect notations (2.5) and (2.6) refer to a $\{10\bar{1}0\}$ plane between two domains having opposing polarity and having stacking mismatch $A \to A$ and $B \to C$. Hence, both D_1 and D_2 are referring to the same defect model. This degeneracy in our notation arises from the periodic repetition of stacking planes parallel to the defect planes.

Now consider the following defect notation,

$$D_3 = \begin{array}{l} \cdots \quad A \quad B \quad \cdots_{(+)} \\ \hline \cdots \quad C \quad B \quad \cdots_{(-)} \end{array}_{\{10\bar{1}0\}} . \tag{2.7}$$

Swapping the stacking labels A and B in (2.7) results in,

$$D_3 = \begin{array}{l} \cdots \quad B \quad A \quad \cdots_{(+)} \\ \hline \cdots \quad C \quad A \quad \cdots_{(-)} \end{array}_{\{10\bar{1}0\}} . \tag{2.8}$$

The right hand side of (2.6) and (2.8) are the same. Which means that D_3 and D_2 (and therefore D_1 as shown previously) refer to the same defect model. Two defect notations will represent two *unique* defects if they are not connected by the operation of interchanging stacking site labels **and/or** they are not equivalent due to periodicity of stacking sequences.

2.2 Inversion domain boundary models

IDBs manifest in the $\{10\bar{1}0\}$ plane. Planar defects in this plane can occur in one of two types, depending on the location of the plane and the proximity of neighboring atoms to the defect plane. As depicted in fig. 2.3, there are sparse $\{10\bar{1}0\}$ planes, conventionally called type 1, and dense $\{10\bar{1}0\}$ planes, called type 2. Our calculations and previous works [30, 62] indicate that for all studied cases of $\{10\bar{1}0\}$ planar defects the type 1 defects are energetically favorable compared to the type 2 defects. Thus, in the rest of this document, unless explicitly stated otherwise any $\{10\bar{1}0\}$ planar defect we discuss or illustrate will be of type 1. Type 2 defects will be distinguished by subscripted 2 in the defect label, for example IDB^*_2 refers to a type 2 IDB* defect.

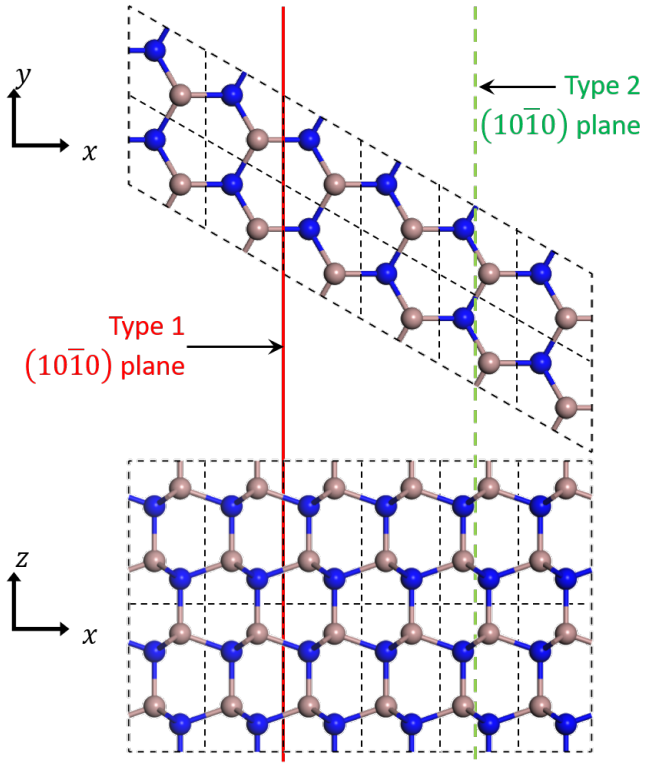

Figure 2.3: Views of (0001)-plane (top) and $(1\bar{2}10)$-plane (bottom) of wurtzite GaN, showing two distinct possible locations for the placement of $(10\bar{1}0)$ defect planes. The plane indicated by the solid red line corresponds to the type 1 $(10\bar{1}0)$ plane and the dashed green line corresponds to the type 2 of the $(10\bar{1}0)$ plane.

Given that IDBs are defined $\{10\bar{1}0\}$ planes separating two domains of opposing polarity, our notation for a generic IDB would be,

$$\frac{\cdots \quad A \quad B \quad \cdots_{(+)}}{\cdots \quad \alpha \quad \beta \quad \cdots_{(-)}} \; _{\{10\bar{1}0\}} \; . \tag{2.9}$$

And the different IDB models correspond to the different possible values for the pair (α, β). Given that α and β take values in the set {A,B,C} and to avoid atomic overlap $\alpha \neq \beta$, there six possible permutations of the pair (α, β). However, only four of these pairs yield *unique* defect models. Two of these correspond to the Holt-IDB and IDB* models described previously. The other two will be labeled IDB′ and IDB″. To the best of our knowledge, IDB′ and IDB″ have not been discussed or evaluated for energetic viability before. Here a $\{10\bar{1}0\}$ defect model is considered to be energetically viable if the domain wall energy is less than twice the $\{10\bar{1}0\}$ surface energy ($\Sigma_{\{10\bar{1}0\}}$).

The four possible IDB models are shown in fig. 2.4, we describe them in more detail here.

i. **Holt-IDB**

$$\frac{\cdots \quad A \quad B \quad \cdots_{(+)}}{\cdots \quad A \quad B \quad \cdots_{(-)}} \; _{\{10\bar{1}0\}} \tag{2.10}$$

Holt-IDB is produced by the interchanging of species sub-lattices in one of the two adjacent domains separated by a $\{10\bar{1}0\}$ plane. Across the defect plane the stacking planes are undisturbed, i.e. stacking planes $A \rightarrow A$ *and* $B \rightarrow B$. Bonds that cross defect plane will be 'wrong bonds' between atoms of the same species as shown in fig. 2.4(a).

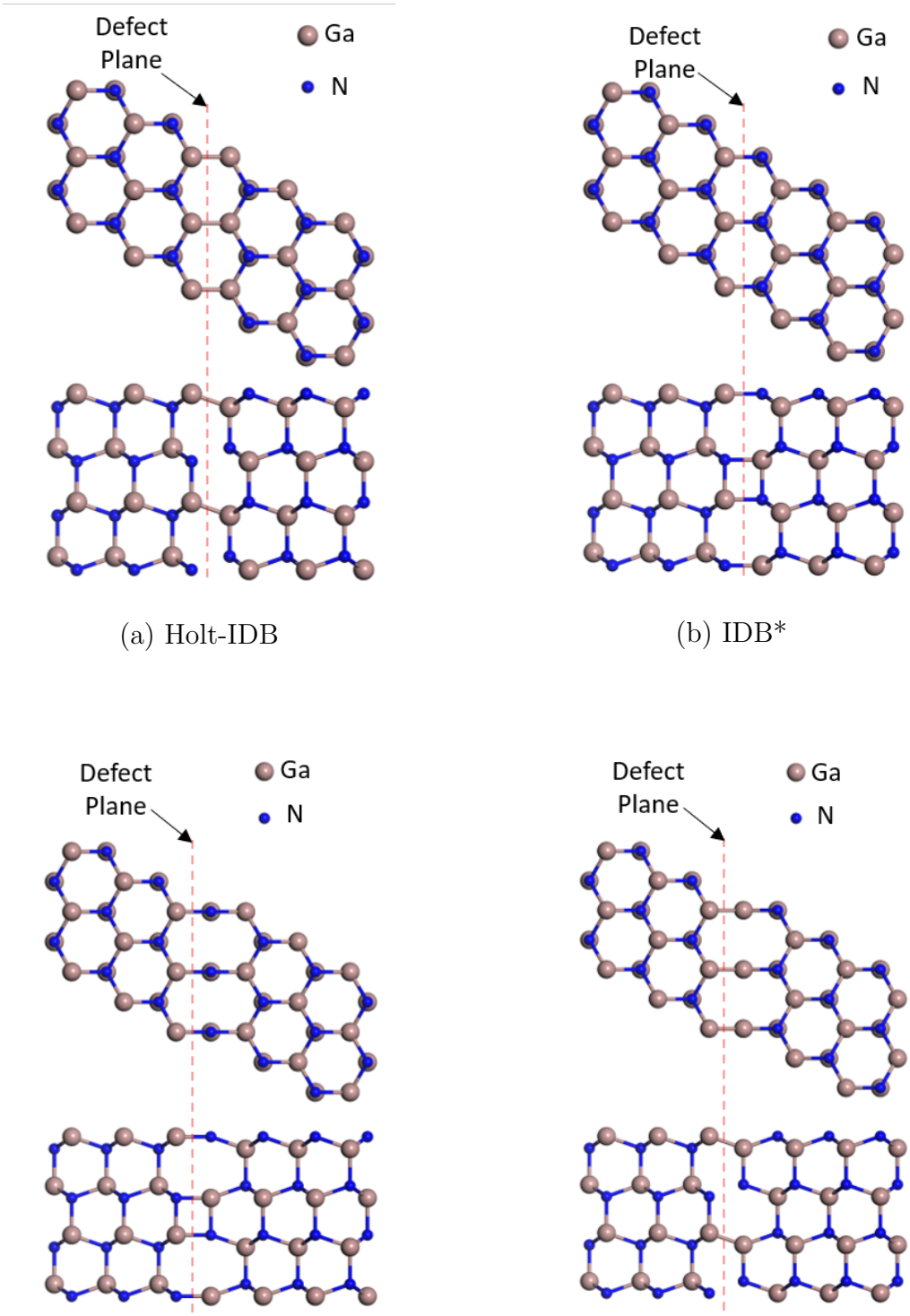

(a) Holt-IDB

(b) IDB*

(c) IDB′

(d) IDB″

Figure 2.4: (0001)-planar (top) and $(1\bar{2}10)$ planar (bottom) views of the indicated inversion domain boundary models.

ii. **IDB***

$$\begin{array}{c} \cdots \quad A \quad B \quad \cdots_{(+)} \\ \hline \cdots \quad B \quad A \quad \cdots_{(-)} \end{array}_{\{10\bar{1}0\}} \tag{2.11}$$

IDB* is produced by introducing a $\frac{1}{2}\mathbf{c}$ relative translation between the two polarity reversed regions in the Holt-IDB model. This translation introduces a mismatch in stacking sequence across the defect plane, i.e. $A \rightarrow B$ *and* $B \rightarrow A$. Bonds across the defect plane are not 'wrong bonds'. Along **c**, the bonds alternately form co-planar four-membered rings and non-co-planar eight-membered rings as depicted in fig. 2.4(b).

iii. **IDB′**

$$\begin{array}{c} \cdots \quad A \quad B \quad \cdots_{(+)} \\ \hline \cdots \quad C \quad A \quad \cdots_{(-)} \end{array}_{\{10\bar{1}0\}} \tag{2.12}$$

From the IDB* model, altering one of the stacking planes in one of the regions to the unoccupied stacking plane location produces the IDB′ defect model. The stacking sequence mismatch in IDB′ can be, $A \rightarrow B$ *and* $B \rightarrow C$ or $A \rightarrow C$ *and* $B \rightarrow A$. The change of stacking to the unoccupied stacking plane location (C here) introduces a net translation of atoms perpendicular to the defect plane. If this translation is away from the defect plane, type 1 IDB′ is formed. If the translation is toward the defect plane, type 2 IDB′ is formed. Similar to IDB* bonds across the defect plane form four-membered and eight-membered rings alternately along **c**. However, the eight-membered rings are asymmetrical. Additionally here, the bonds across the defect plane are not 'wrong bonds' as seen in fig. 2.4(c).

iv. **IDB″**

$$\begin{array}{c} \cdots \quad A \quad B \quad \cdots_{(+)} \\ \hline \cdots \quad A \quad C \quad \cdots_{(-)} \end{array}_{\{10\bar{1}0\}} \tag{2.13}$$

From the Holt-IDB model, altering one of the stacking planes in one of the regions to the unoccupied stacking plane location produces the IDB″ defect model. The stacking sequence mismatch in IDB″ can be, $A \rightarrow A$ *and* $B \rightarrow C$ or $A \rightarrow C$ *and* $B \rightarrow B$. Here also, the change of stacking to the unoccupied stacking plane location (C here) introduces a net translation of atoms perpendicular to the defect plane. And the nature of this translation (away from or toward the defect plane) will determine whether type 1 or type 2 IDB″ is formed. Also here, the bonds across the defect plane are 'wrong bonds' as seen in fig. 2.4(d).

In addition to these IDB models there is another historical model, proposed by Austerman and Gehman [48]. The Austerman model is equivalent to translating the polarity reversed (N polar) region of the IDB* model by $\sim -\frac{1}{8}\mathbf{c}$ such that the Nitrogen sub-lattice is uninterrupted by the defect plane. The motivation for this model was to avoid distorting the sub-lattice corresponding the species with the larger ions. In Beryllium Oxide, for which Austerman's model was proposed, the anions are larger. In the case of GaN the reverse is true and therefore we can conceive a Austerman* model where we do a $\sim +\frac{1}{8}\mathbf{c}$ shift of the polarity reversed region to make the Ga atoms co-planar in (0001) planes. Additionally we can then play the game of changing the relative stacking sequences of the two domains of Austerman and Austerman* models to create a total of eight Austerman based inversion domain boundary models. However, all these models were unstable and found to relax to one of the previously listed four models IDB*, IDB′, Holt-IDB or IDB″.

2.2.1 Stacking Faults

In sec. 2.4 we discuss the transformation of IDBs via interaction with basal stacking faults (SF), hence we provide a brief review of SFs here. SFs occur when the stacking sequence of the GaN crystal is disrupted at a basal plane, i.e. a (0001) plane. Alternately, SFs can be considered as wurtzite-sphalerite transformation for a few atomic layers. Sphalerite also has dimer occupation of stacking planes similar to wurtzite. In the sphalerite structure the stacking sequence has a periodicity of three stacking planes ($\ldots ABCABC \ldots$), unlike the periodic repetition of two stacking planes ($\ldots ABAB \ldots$) of the wurtzite structure. We are aware of three models for SFs described in the literature; they are referred to as I_1 SF, I_2 SF, and E SF. The SF models respectively correspond to three, four, and five basal stacking planes in the sphalerite region. Our calculations for domain wall energies yield $\Gamma_{I_1\,\mathrm{SF}} = 1.1\ m\,eV/\mathring{A}^2$, $\Gamma_{I_2\,\mathrm{SF}} = 2.5\ m\,eV/\mathring{A}^2$, and $\Gamma_{E\,\mathrm{SF}} = 3.9\ m\,eV/\mathring{A}^2$. These values are in agreement with previously reported values [72, 73].

The different SF models can be represented by specifying the stacking sequence in the vicinity of the defect. For example, I_1 SF can be denoted by the sequence $\ldots AB\mathbf{ABC}BC \ldots$. Here the stacking planes given in **bold** correspond to the sphalerite region. SF models have varying thickness depending on the thickness of the sphalerite region, the middle of the sphalerite region is considered to be SF location. If the SF model contains an odd number of stacking planes in the sphalerite region (I_1 SF and E SF), the defect plane location coincides with the central stacking plane in the sphalerite region. We will use a vertical bar (|) to indicate the location of the stacking fault. As such I_1 SF is represented by,

$$\cdots AB\mathbf{AB}|\mathbf{C}BC \ldots . \tag{2.14}$$

If the there are an even number of stacking planes in the sphalerite region the fault

location is in between two stacking planes. So, we denote I_2 SF by,

$$\ldots AB\mathbf{AB}|\mathbf{CA}CA\ldots. \tag{2.15}$$

E SF is is is equivalent to an I_2 SF being immediately followed by an I_1 SF as can be seen from the stacking sequence corresponding to E SF,

$$\cdots AB\underbrace{\overbrace{\mathbf{AB}\text{C}\!\!\!\!\text{C}\mathbf{AB}}^{I_2\ SF}}_{E\ \mathrm{SF}}AB\cdots \tag{2.16}$$

$$\overbrace{\phantom{\cdots AB\mathbf{AB}\text{C}\!\!\!\!\text{C}\mathbf{AB}}}^{I_1\ SF}$$

.

2.3 Methods

2.3.1 Calculating Domain Wall Energies of Defects

We define the domain wall energy of a defect as,

$$\Gamma_{\text{defect}} = \frac{E_{\text{supercell with defects}} - E_{\text{reference}}}{A_{\text{defect}}} \tag{2.17}$$

where, $E_{\text{supercell with defects}}$ is the total energy of a supercell containing the defect, A_{defect} is the area of the defect in the defect supercell, and $E_{\text{reference}}$ is the total energy of a reference supercell that contains an equal number of atoms as the defect supercell.

The sizes of the supercells we create will be denoted by $n_a \times n_b \times n_c$, where n_a, n_b and n_c are the number of repeated primitive unit cells of wurtzite GaN along the **a**, **b**

and **c** directions. When creating defect supercells, the periodicity of the supercells dictate that at least two defect planes are present. We attempt to minimize interaction of defect planes by creating supercells with six primitive unit cells between defect planes. We performed calculations using larger defect supercells, with larger defect plane separation (up to nine primitive unit cells between defect planes). The results indicate that domain wall energies are converged with respect to defect plane separation for supercells six primitive unit cell defect plane separation. This requirement corresponds to the $\{10\bar{1}0\}$ defect planes having a perpendicular separation of $6a\cos(\pi/6)$.

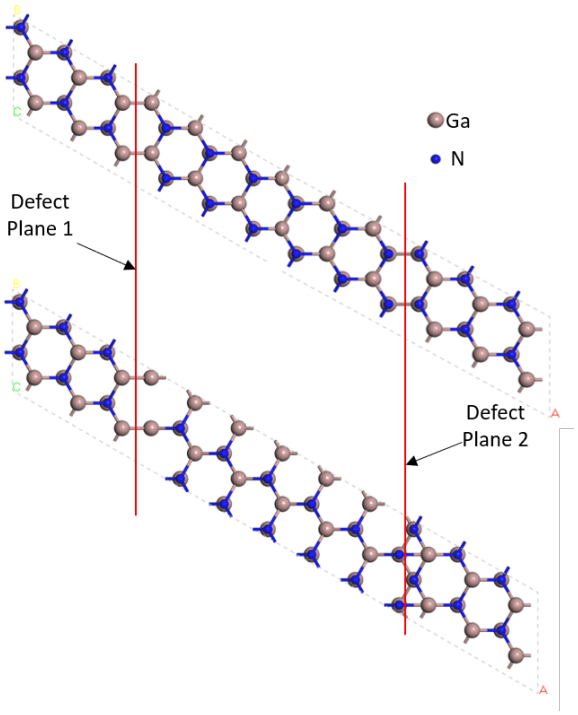

Figure 2.5: (0001) planar views of $12 \times 2 \times 1$ supercells containing, two Holt-IDBs (top) and two IDB″s (bottom). In both the cases the $(01\bar{1}0)$ planar defects are separated by $6a\cos(30^\circ)$.

The definition of Γ_{defect} in (2.17) assumes the defect supercell under consideration contains only one type of defect. However, for $\{10\bar{1}0\}$ planar defects that include all three stacking locations (IDB′, IDB″, and SMB), creating defect supercells containing two defect planes of the same configuration is impossible. Occupying the third stacking

location across the defect plane results in a net translation of atoms perpendicular to the defect plane. This results in one of the planes being the sparse form and the other plane being the dense form of the same defect model. To illustrate this complication, we show (0001)-planar views of $12 \times 2 \times 2$ supercells containing Holt-IDB and IDB$''$ in fig. 2.5. Defect planes 1 and 2 for the Holt-IDB containing supercell are identical with a $\frac{1}{2}\mathbf{c}$ relative shift between them.

Thus, the supercell containing Holt-IDB shown in fig. 2.5 can be used with (2.17). However, the defect planes 1 and 2 in the IDB$''$ containing supercell are not the same type and in fact respectively correspond to the type 1 and type 2 forms of the IDB$''$ defect model. Using this supercell with (2.17) will give the average domain wall energy of the type 1 IDB$''$ and type 2 IDB$''$ models.

For the IDB$'$, IDB$''$, and SMB defects, it is possible to create supercells with only one version of defect *if* six defect planes are included. However, since each defect plane involves a translation of atoms perpendicular to the plane the volume per atom in the defect supercell will be different from the volume per atom of pristine GaN.

In fig. 2.5 we see that a single defect plane translates a GaN dimer $\frac{1}{3}\mathbf{a}$ away from (towards) the boundary for the type 1 (type 2) defect. Since a GaN primitive unit cell has two GaN dimers, over six defect planes, both GaN dimers are translated by $\mathbf{a}$. Therefore, for type 1 (type 2) of each model we create a supercell that occupies the volume of $37(35) \times 1 \times 1$ primitive unit cells and contains the same number of atoms in 36 primitive unit cells. For the reference supercell we create a $36 \times 1 \times 1$ pristine supercell so that the total number of atoms are the same. See fig. appx.2 showing supercell used to determine domain wall energy of IDB$'$.

Table 2.2: Table of size of supercells considered and corresponding k-point grids used.

Supercell Size $(n_a \times n_b \times n_c)$	Monkhorst-Pack k-point grid
$1 \times 1 \times 1$	$9 \times 9 \times 5$
$12 \times 1 \times 1$	$1 \times 9 \times 5$
$(36 \pm n) \times 1 \times 1$ [a]	$1 \times 9 \times 5$

[a] $n = 0, \pm 1$

2.3.2 Computational details

We employed Density Functional Theory (DFT) calculations using the Vienna Ab-initio Simulation Package (VASP) [74, 75]. The exchange correlation interactions were treated using the generalized gradient approximation (GGA) with the Perdew-Burke-Ernzerhof (PBE) functional [76]. The projector augmented wave (PAW) potentials [77,78] recommended and provided by the VASP code were used to treat core states. We use pseudopotentials with valence electron configurations $3d^{10}4s^24p^1$ for Ga and $2s^22p^3$ for N. The cutoff energy and k-point mesh were chosen such that the calculated total energies of the supercells of interest were accurate to 1 m eV. For this, we chose a cutoff energy of 900 eV. The k-point meshes used to sample the reciprocal space were Monkhorst-Pack grids [79] centered at the Gamma point. The k-point meshes were automatically generated using the VASP scheme to generate k-point meshes by specifying a length parameter (R_k). This grid scheme produces, $N_i = int(max(1, R_k \times |\vec{b}_i| + 0.5))$ divisions along each reciprocal lattice vector ($\{\vec{b}_i\}$). Table 2.2 lists the resulting k-mesh grids used depending on the supercell size.

Table 2.3: Domain wall energies of type 1 and type 2 defect models for IDB models. For type 1 models if available literature values are listed.

Defect Model	Domain Wall Energy, Γ (m eV/Å^2)		
	Type 1	Literature value	Type 2
Holt-IDB	195.2	167 [33]	253.2 [a]
IDB*	17.7	25 [33]	44.7
IDB′	131.6	-	172.4
IDB″	246.3 [a]	-	392.9 [a]

[a] These Γ values do not satisfy the energetic viability condition, $\Gamma < 2\Sigma_{\{10\bar{1}0\}}$.

2.4 Discussion

The domain wall energies of the $\{10\bar{1}0\}$ planar IDB models are listed in table 2.3. Each model is evaluated for energetic viability by the condition $\Gamma < 2\Sigma_{\{10\bar{1}0\}}$, according to our calculations $\Sigma_{\{10\bar{1}0\}} = 98.7$ m eV/Å^2.

Of the IDB models, IDB″ and type 2 Holt-IDB fail the viability test and can be discarded. Northrup's IDB*, type 1 and type 2, has significantly lower domain wall energy compared to the other models and is confirmed to be the preferred configuration for IDBs. The IDB′, although energetically unfavorable compared IDB*, is physically viable and may occur in GaN samples. During epitaxial growth of GaN samples, in some cases, the formation of IDB′ may be kinetically favored.

One possible example of IDB′ forming can be found in the work of Kong et al. [28]. This work studies the formation of inversion domains in GaN nano-columns grown using MBE on Titanium (Ti) masked GaN substrates. The authors attribute the formation of inversion domains to a residual (0001) Ti monolayer at the base of the inversion domains. Various configurations of the interfacial TiN monolayer and the subsequent growth of the

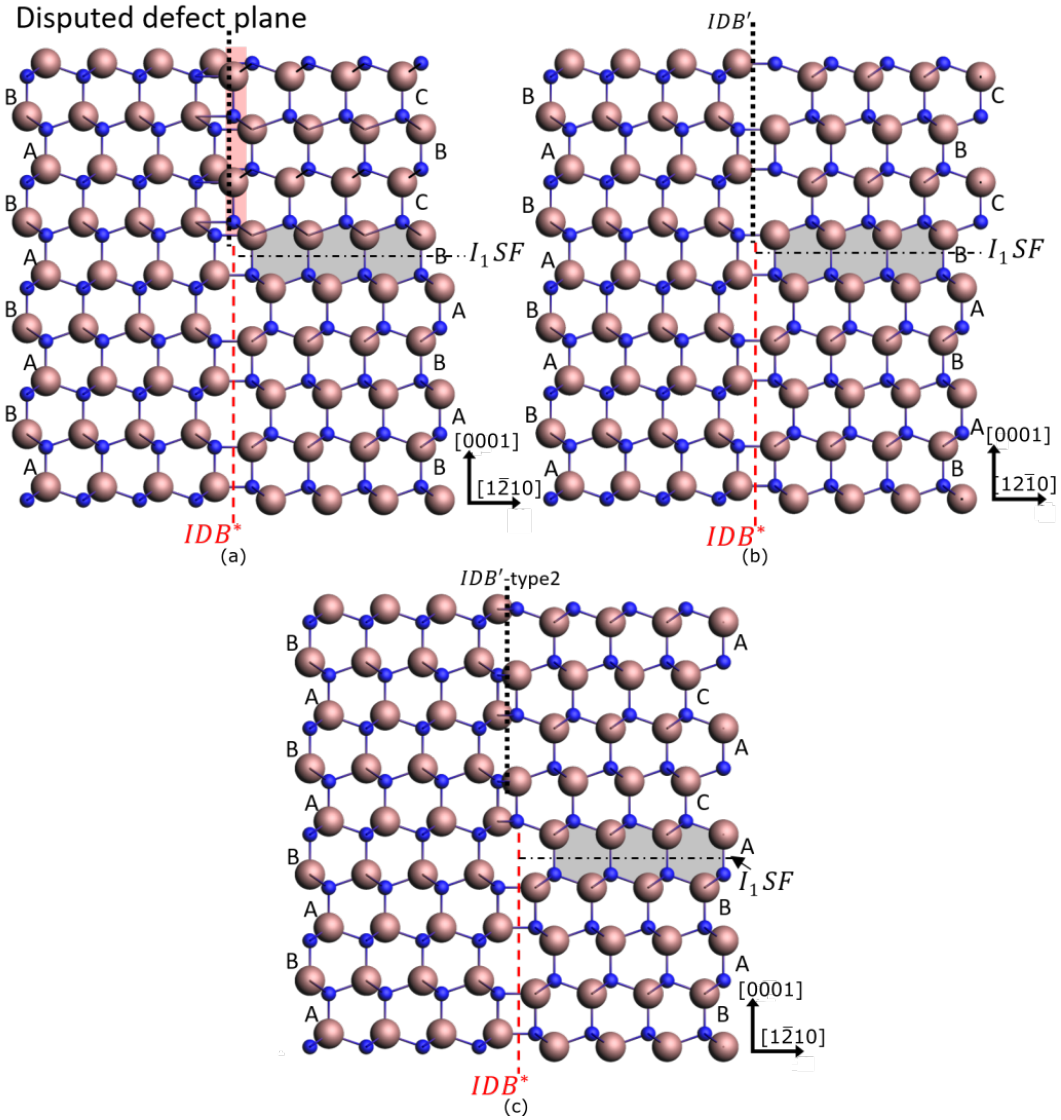

Figure 2.6: (a) Previously proposed atomic model for the IDB*–I_1 SF interaction, (b) Atomic model resulting from removal of spurious atoms (highlighted by the region shaded red in (a)) in the previously proposed model, and (c) IDB*–I_1 SF interaction with I_1 SF shifted by $\frac{1}{2}\mathbf{c}$ such that the SF plane is terminated by an eight-membered ring of IDB*.

polarity inverted region are studied. In the lowest energy Ti monolayer configuration (see Fig. 6 of [28]), the stacking sequence mismatch between the inversion domain and the nano-column matrix corresponds to the stacking sequence mismatch of IDB′. Therefore we expect IDB′ defects to be found at the boundary of the Ti monolayer.

The most compelling argument for the possible existence of IDB′ is found in works [59–62] studying the transformation of IDB* via an interaction with an I_1 Stacking Fault (I_1 SF). The authors identify the IDB resulting from the IDB*— I_1 SF interaction as the Holt-IDB model. They provide the atomic model shown in fig. 2.6(a) (Fig. 11c in [61] and fig. 3b in [60]) to justify this claim. We can extend our notation to analyze the combined defects shown in fig. 2.6(a, b). The notation for this atomic model will be,

$$\begin{array}{c} \cdots \quad A \quad B \quad A \quad B \quad A \quad B \quad A \quad B \quad \cdots_{(+)} \\ \hline \\ \cdots \quad B \quad A \quad B \quad \mathbf{A} \quad \mathbf{B} \quad \mathbf{C} \quad B \quad C \quad \cdots_{(-)} \end{array} \quad _{\{10\bar{1}0\}} \ . \tag{2.18}$$

Note, the notation is oriented rotated 90° clockwise with respect to the atomic model images. The stacking sequence mismatch across the $\{10\bar{1}0\}$ plane, to the right of the SF plane in (2.18) (above the SF plane in fig. 2.6(a-c)), is the same as the stacking sequence mismatch of IDB′ ($A \rightarrow B$ and $B \rightarrow C$) and not that of the Holt-IDB ($A \rightarrow A$ and $B \rightarrow B$). Consequently, we propose that the correct interpretation of this image is that the SF transforms a IDB* defect into an IDB′.

We assume that the erroneous interpretation derives from the fact that the authors did not know about IDB′ at the time of writing their works. Moreover, the atomic model proposed by the authors (fig. 2.6(a)), has a high density of atoms at the interface. We have identified the spurious atoms (enclosed in the shaded region of fig. 2.6(a)) that cause this increase in density. The model obtained by removing the spurious atoms shown in fig. 2.6(b); and here the disputed defect plane corresponds exactly to the proposed IDB′ structure (fig. 2.4(c)). We also notice that if the SF is shifted by $\frac{1}{2}\mathbf{c}$, the resulting defect would be an IDB′-type 2. In this scenario (fig. 2.6(c)), the SF is terminated by an 8 member ring, as opposed to the four member ring of fig. 2.6(a).

The IDB*— I_1 SF interaction was proposed as a possible explanation for experimental observations of Holt-IDB in GaN samples [61, 62]. As we have shown the IDB*— I_1 SF interaction results in IDB′ and thus cannot explain the observations of Holt-IDBs. Nevertheless, we can look at the other SF models described in sec. 2.2.1 and their interaction with IDB* to explain the formation of Holt-IDBs. We analyze the IDB*— SF model interactions with the aid of our notation. Note the notation does not differentiate between atomic models that have different SF locations and/or include spurious atoms (i.e. (2.18) represents all models shown in fig. 2.6); these considerations must be treated according to our discussion in the preceding paragraph.

The IDB*– I_2 SF interaction can be represented in our notation as,

$$\begin{array}{c} \cdots \quad A \quad B \quad A \quad B \quad A \quad B \quad A \quad B \quad A \quad \cdots_{(+)} \\ \hline \cdots \quad B \quad A \quad B \quad \mathbf{A} \quad \mathbf{B} \,|\, \mathbf{C} \quad \mathbf{A} \quad C \quad A \quad \cdots_{(-)} \end{array}_{\{10\bar{1}0\}} . \tag{2.19}$$

Now the stacking sequence mismatch of the transformed $\{10\bar{1}0\}$ plane (right of SF plane in (2.19)) is the same as IDB'' ($A \rightarrow A$ and $B \rightarrow C$). However, as we have stated previously IDB'' is energetically not viable and is unlikely to appear in GaN samples. This impasse can be resolved in one of two ways. The first would be to remove the I_2 SF by introducing a $1/3 < 1\bar{1}00 >$ basal shear at the I_2 SF plane. This is feasible since I_2 SF is the only SF model that can be formed (or removed) through strain relaxation. In this scenario removing the I_2 SF results in no transformation of the IDB*. The second way of avoiding forming IDB'' is to include one more stacking plane in the sphalerite

sequence, i.e. $I_2\ SF$ becomes $E\,SF$. This scenario can be denoted by,

$$\begin{array}{l} \cdots\ \ A\ \ B\ \ A\ \ B\ \ A\ \ B\ \ A\ \ B\ \ A\ \ B\ \cdots_{(+)} \\ \hline\hline \\ \cdots\ \ B\ \ A\ \ B\ \ \mathbf{A}\ \ \mathbf{B}\ \ \mathbf{\mathbb{C}}\ \ \mathbf{A}\ \ \mathbf{B}\ \ A\ \ B\ \cdots_{(-)} \end{array} \quad \{10\bar{1}0\}\ . \tag{2.20}$$

Now the stacking sequence mismatch of the transformed$\{10\bar{1}0\}$ defect is consistent with Holt-IDB ($A \rightarrow A$ and $B \rightarrow B$). Hence, it is possible for IDB* to transform to the Holt-IDB only when interacting with an $E\,SF$.

The work by Lançon et al. [80] studies picometer-scale inter-domain shifts parallel to the polarization axis, in supercells containing IDB*. In the IDB* structure, atomic layers in basal planes are occupied by opposing species (i.e. Ga $\rightarrow$ N or N $\rightarrow$ Ga) across the defect plane. Lançon et al. define the inter-domain shift (δz) as, the difference the between the **c**-axis coordinate of a Ga atom basal plane in the Ga-polar domain and the corresponding N atomic plane in the N-polar domain. In the IDB* structure proposed by Northrup et al. [33], prior to geometry optimization, $\delta z_{initial} = 0$. Lançon et al. note that when an initial inter-domain shift ($\delta z_{initial} > \ 3.1\,\text{pm}$) is introduced, the structure relaxes to a configuration with a final inter-domain shift $\delta z = 8$ pm. If no initial inter-domain shift is introduced the relaxed configuration has an inter-domain shift $\delta z = -1$ pm. Further, Lançon et al. show that the relaxed configuration with $\delta z = 8\,pm$ is energetically favorable. They conclude that IDB* as proposed by Northrup et al. is a meta-stable configuration and the actual IDB* ground state is only reached when an initial inter-domain shift is introduced. The findings of Lançon et al. are experimentally corroborated by experimental measurements of inter-domain shifts in GaN nanowires containing IDBs, measured by Bragg Coherent X-ray imaging [63, 64]. The relaxed IDB′ structure, that we propose, could also be sensitive picometer-scale inter-domain shifts to

the initial configuration. Further calculations are necessary to determine if the relaxed structure of IDB′ is sensitive to picometer scale translations between domains in the original structure.

In conclusion, in this chapter we present a notation to characterize IDBs based on the stacking sequence mismatch between the polarity inverted domains. With the aid of this notation we propose two new IDB models that have not been previously reported on. We perform ab-initio DFT calculations to estimate the domain wall energies of IDB models and assess energetic viability. One of the IDB models that we propose - IDB′ - is energetically viable and has a domain wall energy that is lower than the Holt-IDB, but higher than the preferred IDB configuration IDB*. We provide an alternate explanation for previous experimental interpretation of TEM imagery of IDB*– I_1 SF interactions. We propose IDB′ as the most suitable to describe the defect plane arising from this interaction over the previous interpretation that identified this defect as Holt-IDB. Additionally we analyze IDB* interacting with other SF models. This analysis yields a possible scenario for the formation of Holt-IDB via an IDB*– E SF interaction.

The IDB′ and IDB″ models that we propose in this chapter are valid models for IDBs in other materials that have the wurtzite crystal structure. Further our notation can be used to characterize other planar defects in the wurtzite crystal structure. Our notation can be used to denote planar defects that lie in planes parallel to the macroscopic polarization, such as: stacking mismatch boundaries, $\{\bar{1}2\bar{1}0\}$-IDBs, and prismatic stacking faults. We present an analysis of these defects and possible models in the following chapter.

Chapter 3

IDBs and other planar defects in wurtzite materials.

3.1 Introduction

In this chapter we evaluate the energetic viability of the newly proposed IDB models (in chap. 2) in Aluminum Nitride, Boron Nitride, Zinc Oxide, and Zinc Sulphide. Further we extend our notation to propose models for other planar defects in wurtzites. The planar defects we are interested in result from a plane delineating two domains that have mismatch in stacking plane alignments and/or inverted polarity. Planar defects that fit this description and belong to planes parallel to the polarization axis (referred to as prismatic planes) are amenable to be denoted with our notation. Recall the notation for a generic defect provided in (2.4),

$$\frac{\cdots \quad A \quad B \quad \cdots_{(+)}}{\cdots \quad \alpha \quad \beta \quad \cdots_{sign(u)}} \quad \cdots\{hklm\}. \tag{3.1}$$

Table 3.1: Defect plane nomenclature based on orientation and relative polarity between domains.

Defect plane $\{hklm\}$	Polarity Inverted Defect	Polarity Aligned Defect
$\{10\bar{1}0\}$	Inversion Domain Boundary (IDB)	Stacking Mismatch Boundary (SMB)
$\{\bar{1}2\bar{1}0\}$	$\{\bar{1}2\bar{1}0\}$-planar Inversion Domain Boundary (aIDB)	Prismatic Stacking Fault (PSF)

For one of the domains - delineated by the defect plane - we assign the stacking sequence $\cdots AB \cdots$. Further, in an infinite crystal one may redefine the crystal **c**-axis such that the first domain is Ga-polar, i.e. $u > 0$. The planar defects of interest can be classified into categories based on the orientation of defect plane, and polarity of the second domain. The various possibilities for stacking plane mismatch between the domains result in different models for each category of defects. Further, the spontaneous polarization of the second domain can either be aligned with or opposite the polarity of the first domain. There are two high symmetry prismatic planes we consider for defect planes. They are the $\{10\bar{1}0\}$-plane also referred to as the hexagonal m-plane, and the $\{\bar{1}2\bar{1}0\}$ also referred to as the hexagonal a-plane.

Hence, the defect planes we investigate can be classified into four categories based on defect plane orientation, relative stacking sequence, and the alignment of polarity between the domains on either side of the separating plane. The defect categories and historical nomenclature used to refer to said defects are listed in table 3.1. We also extend our exploration to other materials that exhibit the wurtzite crystal structure. Materials with technological interest for device applications such as Aluminum Nitride (AlN), Boron Nitride (BN), Zinc Oxide (ZnO), and Zinc Sulphide (ZnS) are chosen as candidate materials.

3.1.1 Methods

Given the multitude of defect categories and associated models to be studied, efficient usage of computational resources is a priority. As such we have tweaked our computational parameters, compared to chap. 2, to reduce computational cost while maintaining an acceptable level of accuracy. A detailed analysis of the changes to computational parameters is presented in the appendix. To summarize, for each material we have chosen a lower cutoff energy, equal to 1.3 times the maximum ENMAX value provided in the pseudopotential files of the constituent atomic species. Further to have more consistency between calculations Γ-centered k-point meshes were produced by specifying the number of k-points to sample along each reciprocal lattice vector. Here, the number of points in each reciprocal lattice direction were chosen by limiting the maximum k-point separation. For the candidate materials the cutoff energies, maximum k-point separation, and relaxed cell parameters for the relaxed primitive unit cells are reported in table 3.2. The pseudopotentials recommended by VASP (see `https://www.vasp.at/wiki/index.php/Available_PAW_potentials`) were used to treat core states. The pseudopotential file used for each atomic species and corresponding valence electron configurations are listed in table appx.1.

Table 3.2: Choice of Cutoff Energy, Maximum k-point separation, resulting relaxed cell parameters.

Material	Cutoff Energy (eV)	Maximum k-point separation ($Å^{-1}$)	Primitive unit cell constants			
			a (Å)	c (Å)	c/a	u
AlN	520	0.30	3.13	5.02	1.603	0.381
BN	520	0.35	2.56	4.23	1.654	0.375
GaN	520	0.35	3.20	5.22	1.629	0.377
ZnO	520	0.25	3.29	5.31	1.615	0.379
ZnS	360	0.25	3.85	6.30	1.637	0.375

The defect supercells for the $\{10\bar{1}0\}$ defects can be created by repeating the primitive wurtzite unit cell, as done in the previous chapter. However, the $\{\bar{1}2\bar{1}0\}$-planar defects require supercells created by repetition of a different conventional unit cell. The reason supercells built from primitive unit cells are unsuitable for the $\{\bar{1}2\bar{1}0\}$-planar defects is, $\{\bar{1}2\bar{1}0\}$ does not coincide with any of the primitive unit cell faces. This leads to $\{\bar{1}2\bar{1}0\}$-planar defects being discontinuous constructed in a supercell of the primitive unit cell when the supercell is repeated periodically. This scenario is schematically illustrated in fig. 3.1.

As shown in fig. 3.1(a) $(10\bar{1}0)$ coincides with a primitive unit cell face whilst $(\bar{1}2\bar{1}0)$ does not. As such, in supercells of the primitive unit cell (fig. 3.1(b)), the $(10\bar{1}0)$ plane is continuous and the $(\bar{1}2\bar{1}0)$ plane is discontinuous. The periodic repetition of this supercell illustrates the discontinuity of the $\{\bar{1}2\bar{1}0\}$ (fig. 3.1(c)). In order to construct supercells that have continuous $\{\bar{1}2\bar{1}0\}$ planes, we use the conventional unit cell shown in fig. 3.1(d). Here, since $(\bar{1}2\bar{1}0)$ coincides with one of the unit cell faces, supercells constructed by repeating this unit cell will have continuous $\{\bar{1}2\bar{1}0\}$ planes.

An important consideration when computing domain wall energies, is the convergence of domain wall energies with respect to domain wall separation. Exhaustively checking for convergence of domain wall energies with respect to defect plane separation is infeasible due to computational cost. For the $\{10\bar{1}0\}$-planar defects, the defect plane separations was deemed to be sufficient if the IDB* model domain wall energies were converged. As such, defect supercells were constructed such that the defect planes were separated by six primitive unit cells. This corresponds to $6a\cos(30^\circ)$ perpendicular distance between defect planes. This defect plane separation was found to be sufficient to converge domain wall energies with respect to defect plane separation, for all IDB models in GaN.

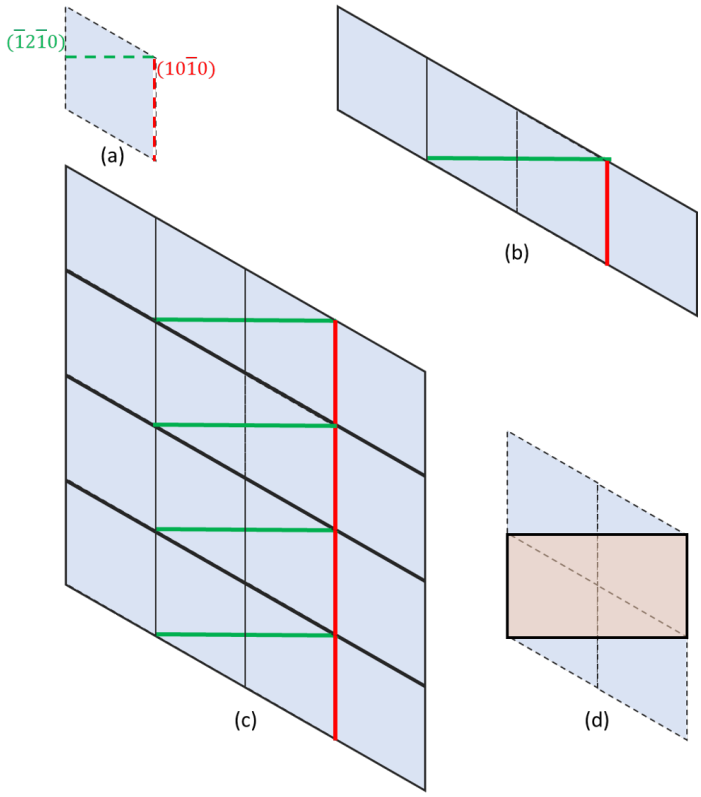

Figure 3.1: (0001)-planar schematic representations of:
(a) A wurtzite primitive unit cell showing the orientation of $\{10\bar{1}0\}$ (red dashed line) and $\{\bar{1}2\bar{1}0\}$ (green dashed line) planes.
(b) A supercell built by $4 \times 1 \times 1$ repetitions of the primitive unit cells containing hypothetical planar defects in the $\{10\bar{1}0\}$-plane (solid red line) and the $\{\bar{1}2\bar{1}0\}$-plane (solid green line),
(c) A larger supercell built by $1 \times 4 \times 1$ repetitions of the supercell shown in (b); here the $\{10\bar{1}0\}$-planar defect is continuous, however the $\{\bar{1}2\bar{1}0\}$-planar defect is interrupted by the unit cell boundary and is discontinuous.
(d) A conventional unit cell (bounded by solid black line) for the wurtzite structure where $\{\bar{1}2\bar{1}0\}$ is one of the unit cell faces. Supercells of this unit cell allow for creation of continuous $\{\bar{1}2\bar{1}0\}$-planar defects.

Similarly, for the $\{\bar{1}2\bar{1}0\}$-planar defects, the defect plane separations were considered sufficient if the aIDB* domain wall energy of GaN is converged. Hence, in the $\{\bar{1}2\bar{1}0\}$ planar defect supercells defect planes were separated by six conventional unit cells shown in fig. 3.1(d). This corresponds to $6a$ perpendicular distance between defect planes in the $\{\bar{1}2\bar{1}0\}$-planar defect supercells.

Table 3.3: $\{10\bar{1}0\}$ and $\{\bar{1}2\bar{1}0\}$ planar surface energies for the wurtzite materials studied.

Material	$\Sigma_{\{10\bar{1}0\}}$ $\left(\text{m eV/Å}^2\right)$	$\Sigma_{\{\bar{1}2\bar{1}0\}}$ $\left(\text{m eV/Å}^2\right)$
AlN	134	139
BN	122	137
GaN	98	103
ZnO	53	56
ZnS	24	23

As in the previous chapter a planar defect can be considered to be energetically viable if the domain wall energy is less than twice the defect plane surface energy (Σ). In all materials, for both $\{10\bar{1}0\}$ and $\{\bar{1}2\bar{1}0\}$ surfaces, a vacuum thickness of 12Å was found to be sufficient to converge the surface energy with respect to vacuum thickness. Table 3.3 lists the surface energies of the planes of interest for all the materials studied.

3.2 Inversion domain boundaries in wurtzite hexagonal m-planes.

In table 2, we presented two new models (IDB′ and IDB″) for $\{10\bar{1}0\}$-planar inversion domain boundaries. Here, we will assess the viability of these models and compare their domain wall energies to existing models (IDB* and Holt-IDB). Recall the definition of an IDB - a $\{10\bar{1}0\}$ plane separating two domains which have opposing polarity. The notation for a generic IDB was given in (2.9),

$$\begin{array}{c} \cdots \quad A \quad B \quad \cdots_{(+)} \\ \hline \cdots \quad \alpha \quad \beta \quad \cdots_{(-)} \end{array}_{\{10\bar{1}0\}} . \tag{3.2}$$

The different models for IDBs correspond to the different possible permutations of the values of this notation. We established, there are four possibilities for the pair (α, β),

and hence we have four possible IDB models. The IDB models listed below in order of increasing domain wall energies. A detailed description of these models and accompanying images can be found in sec. 2.2.

- IDB* : $\dfrac{\cdots \quad A \quad B \quad \cdots_{(+)}}{\cdots \quad B \quad A \quad \cdots_{(-)}} \ \{10\bar{1}0\}$.
- IDB′ : $\dfrac{\cdots \quad A \quad B \quad \cdots_{(+)}}{\cdots \quad C \quad A \quad \cdots_{(-)}} \ \{10\bar{1}0\}$.
- Holt-IDB: $\dfrac{\cdots \quad A \quad B \quad \cdots_{(+)}}{\cdots \quad A \quad B \quad \cdots_{(-)}} \ \{10\bar{1}0\}$.
- IDB″ : $\dfrac{\cdots \quad A \quad B \quad \cdots_{(+)}}{\cdots \quad A \quad C \quad \cdots_{(-)}} \ \{10\bar{1}0\}$.

Table 3.4 shows the calculated domain wall energies for each of the IDB models in the wurtzite materials we studied. From the reported results we see that IDB* is the thermodynamically preferred structure for IDBs in all materials. IDB′ is also energetically viable in all materials and is expected to exist in wurtzite samples when growth kinetics favor its formation. The Holt-IDB is viable in GaN only, in other materials the structure is either energetically unviable or relaxes to the IDB* structure. Hence, the Holt-IDB structure is not expected to be found in wurtzite samples other than GaN. Similarly, IDB″ is universally unviable and not expected to be found in nature. Looking at the IDBs in the type 2 $\{10\bar{1}0\}$-plane, IDB*$_2$ is universally viable and the preferred structure. IDB$'_2$ is energetically viable in some cases. The other two models Holt-IDB$_2$ and IDB$''_2$ are unviable or unstable in all cases.

Table 3.4: Domain wall energies for IDB models in Wurtzites.

	Type 1 Defects Γ (m eV/Å^2)				Type 2 Defects Γ (m eV/Å^2)			
	IDB*	IDB′	Holt	IDB″	IDB*$_2$	IDB′$_2$	Holt$_2$	IDB″$_2$
AlN	14	164	IDB* [b]	411 [a]	40	183	464 [a]	IDB′$_2$ [b]
BN	48	231	322 [a]	421 [a]	116	336 [a]	517 [a]	523 [a]
GaN	18	132	196	246 [a]	45	173	255 [a]	IDB′$_2$ [b]
ZnO	9	67	IDB* [b]	IDB′ [b]	21	81	IDB*$_2$ [b]	IDB′$_2$ [b]
ZnS	8	46	IDB* [b]	132 [a]	18	68 [a]	167 [a]	IDB′$_2$ [b]

[a]These Γ values do not satisfy the energetic viability condition, $\Gamma < 2\Sigma_{\{10\bar{1}0\}}$.
[b]These models were unstable, and relaxed to the indicated structure.

3.3 Inversion domain boundaries in wurtzite hexagonal a-planes.

$\{\bar{1}2\bar{1}0\}$-planar inversion domain boundaries (aIDB) are defined as a $\{\bar{1}2\bar{1}0\}$ plane separating two domains with opposing polarity. The notation we present in (2.4) can be adapted to treat aIDBs. Similar to the $\{10\bar{1}0\}$-planar IDBs, the different models of aIDBs correspond to the different possibilities for the relative stacking sequences between the abutting domains. A generic notation for an aIDB can be written as,

$$\frac{\cdots \quad A \quad B \quad \cdots_{(+)}}{\cdots \quad \alpha \quad \beta \quad \cdots_{(-)}} \quad _{\{\bar{1}2\bar{1}0\}} \ . \tag{3.3}$$

Here again, since α and β take values in $\{A, B, C\}$ and $\alpha \neq \beta$ to avoid atomic overlap and therefore there are six possible permutations for the pair (α, β). These six possible pair values result in four *unique* stacking sequence mismatches between the domains of the aIDB. The notations and the labels we will be using to refer to the resulting four

possible models for aIDBs are listed below.

- aHolt

$$\begin{array}{c} \cdots \quad A \quad B \quad \cdots_{(+)} \\ \hline \cdots \quad A \quad B \quad \cdots_{(-)} \end{array}_{\{\bar{1}2\bar{1}0\}} \tag{3.4}$$

  The aHolt model is produced by interchanging the species sub-lattices in one of the two domains separated by a $\{\bar{1}2\bar{1}0\}$ plane. There is no stacking sequence mismatch between the domains. Bonds straddling the plane are 'wrong bonds' between atoms of the same species. This model was found to be unstable under relaxation.

- aIDB*

$$\begin{array}{c} \cdots \quad A \quad B \quad \cdots_{(+)} \\ \hline \cdots \quad B \quad A \quad \cdots_{(-)} \end{array}_{\{\bar{1}2\bar{1}0\}} \tag{3.5}$$

  The aIDB* model is produced by introducing a $1/2\mathbf{c}$ relative translation between the two domains of the aHolt model. This results in a $A \to B$ and $B \to A$ stacking sequence mismatch between the domains. Bonds across the defect plane are not wrong bonds and form alternating co-planar four-membered rings and non-co-planar eight-membered rings along $\mathbf{c}$, as shown in fig. 3.2(a). Unlike in the IDB* model, in aIDB* the plane of the four-membered ring of bonds is not perpendicular to the defect plane.

- aIDB′

$$\begin{array}{c} \cdots \quad A \quad B \quad \cdots_{(+)} \\ \hline \cdots \quad C \quad A \quad \cdots_{(-)} \end{array}_{\{\bar{1}2\bar{1}0\}} \tag{3.6}$$

  From the aIDB* model, altering a stacking plane in one of the domains to the unoccupied stacking plane location, produces the aIDB′ model. The atomic structure of this model is shown in fig. 3.2(b).

- aIDB″

$$\begin{array}{c} \cdots \quad A \quad B \quad \cdots_{(+)} \\ \hline \cdots \quad A \quad C \quad \cdots_{(-)} \end{array}_{\{\bar{1}2\bar{1}0\}} \tag{3.7}$$

Introducing a 1/2 **c** relative translation between the two domains of aIDB′ produces the aIDB″ model. This model was found to be unstable under relaxation.

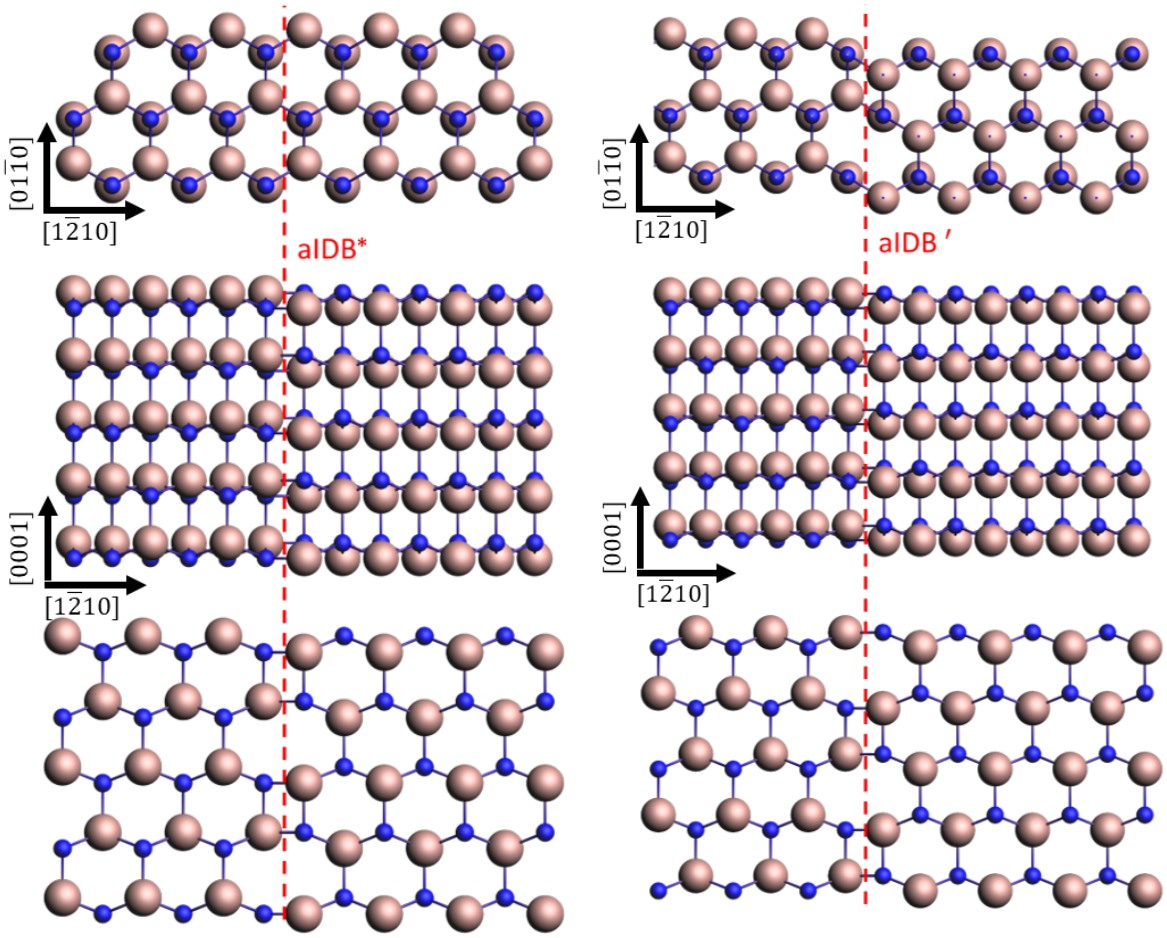

(a) IDB*

(b) aIDB″

Figure 3.2: (top) (0001)-planar view, (center) (10$\bar{1}$0)-planar view, and (bottom)(10$\bar{1}$0)-planar view with depth of view of $|\mathbf{a}|$, allowing for better visualization of bond structure of (a) aIDB* model and (b) aIDB′

Table 3.5: Domain wall energies for aIDB models in Wurtzites.

	Γ (m eV/Å^2)			
	aIDB*	aIDB′	aHolt	aIDB″
AlN	17	75	aIDB*[b]	aIDB*[b]
BN	54	194	363 [a]	492 [a]
GaN	21	76	235 [a]	aIDB*[b]
ZnO	10	38	aIDB*[b]	aIDB*[b]
ZnS	10	31	aIDB*[b]	aIDB*[b]

[a]These Γ values do not satisfy the energetic viability condition, $\Gamma < 2\Sigma_{\{\bar{1}2\bar{1}0\}}$.
[b]These models were unstable, and relaxed to the indicated structure.

Table 3.5 shows the calculated domain wall energies for aIDB defect models. The analysis of calculated domain wall energies of aIDBs is very similar to the discussion for domain wall energies of type-1 IDBs presented in table 3.4. Note $\{\bar{1}2\bar{1}0\}$ can only be in one type unlike $\{10\bar{1}0\}$ which can take two types (type 1 and type 2) depending on the location of the plane. Hence, $\{\bar{1}2\bar{1}0\}$ planar defects such aIDBs (and later prismatic stacking faults) only have one type. aIDB* and aIDB′ are energetically viable in all materials studied, with aIDB* being the preferred structure. aHolt and aIDB″ models in all cases are either energetically unviable or unstable and relax to the preferred structures aIDB*.

3.4 Prismatic stacking faults in wurtzites.

Prismatic stacking faults (PSF) refer to a $\{\bar{1}2\bar{1}0\}$ separates two domains that have the same polarity but mismatched stacking sequence. By adapting our generic defect notation (2.4) to specify PSFs, we get the representation of a generic PSF as,

$$\begin{array}{c} \cdots \quad A \quad B \quad \cdots_{(+)} \\ \hline \cdots \quad \alpha \quad \beta \quad \cdots_{(+)} \end{array}_{\{\bar{1}2\bar{1}0\}} . \tag{3.8}$$

Here again, we consider the possible pair values for (α, β) and obtain four possible *unique* pair values. However, when $(\alpha, \beta) = (A, B)$ the resulting defect is trivial, i.e. there is crystal stacking sequence and polarity are the same on either side of the interface. Rejecting the trivial result, we have three possible models for PSFs. The notations and labels we use to refer to the three possible PSF models are listed below.

- PSF′

$$\begin{array}{c} \cdots \quad A \quad B \quad \cdots_{(+)} \\ \hline \cdots \quad C \quad A \quad \cdots_{(+)} \end{array}_{\{\bar{1}2\bar{1}0\}} \tag{3.9}$$

- PSF″

$$\begin{array}{c} \cdots \quad A \quad B \quad \cdots_{(+)} \\ \hline \cdots \quad A \quad C \quad \cdots_{(+)} \end{array}_{\{\bar{1}2\bar{1}0\}} \tag{3.10}$$

- PSF*

$$\begin{array}{c} \cdots \quad A \quad B \quad \cdots_{(+)} \\ \hline \cdots \quad B \quad A \quad \cdots_{(+)} \end{array}_{\{\bar{1}2\bar{1}0\}} \tag{3.11}$$

Table 3.6: Domain wall energies for PSF models in Wurtzites.

	Γ (m eV/Å^2)		
	PSF″	PSF′	PSF*
AlN	66 (72 [81])	0 [b]	479 [a]
BN	140	0 [b]	436 [a]
GaN	58	0 [b]	279 [a]
ZnO	29	0 [b]	154 [a]
ZnS	22	0 [b]	142 [a]

[a]These Γ values do not satisfy the energetic viability condition, $\Gamma < 2\Sigma_{\{\bar{1}2\bar{1}0\}}$.
[b]This model were unstable, and relaxed to the bulk (i.e. no stacking mismatch between the domains).

Table 3.6 shows the calculated domain wall energies of the PSF models presented. Of these only PSF′ is energetically viable and stable under relaxation. Since we only have one viable model for prismatic stacking faults we can refer to this model as PSF without ambiguity.

3.5 Discussion and Conclusions.

The results for domain wall energies presented in table 3.4 and table 3.5 give us the possible models for IDBs and aIDBs respectively. The possible configurations for IDBs are IDB* and IDB′; with IDB* being the energetically preferred configuration. Similarly, the possible configurations for aIDBs are aIDB* and aIDB′; with aIDB* being the energetically preferred configuration.

The domain wall energies of the preferred structures for inversion domain boundaries in $\{10\bar{1}0\}$ and $\{\bar{1}2\bar{1}0\}$ - Γ_{IDB^*} and Γ_{aIDB^*} respectively - have comparable values in all materials. In fact the ratios between Γ_{IDB^*} and Γ_{aIDB^*} remarkably similar. The same is true for the ratios between Γ_{IDB^*} and $\Gamma_{IDB_2^*}$. The values reported in table 3.4 and table 3.5 are rounded to reflect our confidence with respect to computational parameters; table 3.7 shows the values of $\frac{\Gamma_{aIDB^*}}{\Gamma_{IDB^*}}$ and $\frac{\Gamma_{IDB_2^*}}{\Gamma_{IDB^*}}$ before rounding the individual Γ values. The plots of Γ_{aIDB^*} vs Γ_{IDB^*} and Γ_{aIDB^*} vs Γ_{IDB^*}, shown in fig. 3.3, appears to confirm the linear correlation.

A possible explanation for the consistency of domain wall energy ratios between IDB*, aIDB*, and IDB*$_2$ is the similarity of the bond structures that cross the defect interface in these models. The bonds straddling the defect plane form alternating coplanar fourfold rings and noncoplanar eightfold rings; these rings are identical in all models as can be seen from the bottom panes of fig. 2.4(b), fig. 3.2(a), and fig. 3.4. The difference between the IDB*, aIDB*, and IDB*$_2$ models is the angle at which the (0001)-planar projection of the bonds cross the defect plane, which in turn affects the proximity of atoms adjacent to the interface. The bonds intersect the respective defect planes at 90° for IDB*, 60° for aIDB*, and 30° for IDB*$_2$ as can be seen from the top panes of panes of fig. 2.4(b), fig. 3.2(a), and fig. 3.4. Therefore, atoms adjacent to the

Table 3.7: Ratios of $\frac{\Gamma_{aIDB^*}}{\Gamma_{IDB^*}}$ and $\frac{\Gamma_{IDB_2^*}}{\Gamma_{IDB^*}}$

Material	$\frac{\Gamma_{aIDB^*}}{\Gamma_{IDB^*}}$	$\frac{\Gamma_{IDB_2^*}}{\Gamma_{IDB^*}}$
AlN	1.162	2.743
BN	1.138	2.425
GaN	1.167	2.524
ZnO	1.156	2.422
ZnS	1.176	2.218
Mean value	1.16	2.47
Standard deviation	0.013	0.170

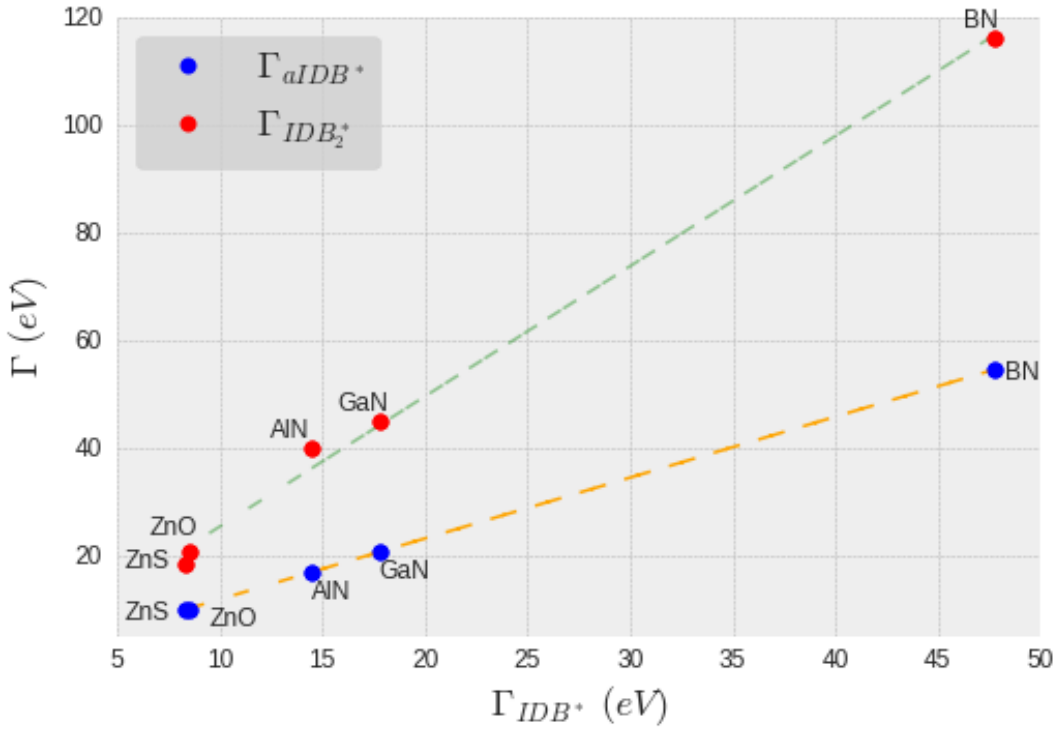

Figure 3.3: Plots of Γ_{aIDB^*} vs Γ_{IDB^*} and $\Gamma_{IDB_2^*}$ vs Γ_{IDB^*}.

boundary are closer for IDB*$_2$, next closest for aIDB*, and finally furthest for IDB*. This in turn explains the difference in domain wall energies for between these models, despite having identical bond structure.

In order of increasing domain wall energy the list of viable models for inversion domain boundaries in wurtzites are: IDB*, aIDB*, aIDB′, and IDB′ (Holt-IDB is viable only in GaN). Experimental evidence for the existence of IDB* in wurtzites is well documented [46, 47, 82]. In sec. 2.2, we discussed the evidence for IDB′ model existing in GaN samples. Even the Holt-IDB model has been found to exist in GaN samples [46, 47, 49]. Given that aIDBs - aIDB* and aIDB′ - have lower domain wall energies than IDB′ and Holt-IDB in all materials studied, we would expect these aIDB models to also exist in samples. However, to the best of our knowledge, discussions of $\{\bar{1}2\bar{1}0\}$-planar IDBs are not found in existing literature. Nonetheless, we do find an example of the possible observation - albeit unacknowledged - of aIDBs in the work of Li et al [64].

Li et al. map inversion domain boundaries in n-doped GaN nanowires using Bragg coherent X-ray diffraction imaging. From the Bragg coherent X-ray diffraction measurements they produce real space reconstruction of phase at different heights along the nanowires, as shown in fig. 3.5(A). The cross-sections show two domains (colored pink and green) of constant phase values. The domains correspond to the Ga-polar (green) and N-polar (pink) regions of the wire. The interior boundaries between the domains are IDBs.

In fig. 3.5(B) we annotate the orientation of the inversion domain boundary planes as either $\{10\bar{1}0\}$-planes (black lines) or $\{\bar{1}2\bar{1}0\}$-planes (white lines). In the (0001)-plane, the orientation of the black lines are limited to integer multiples of 60° from the horizontal

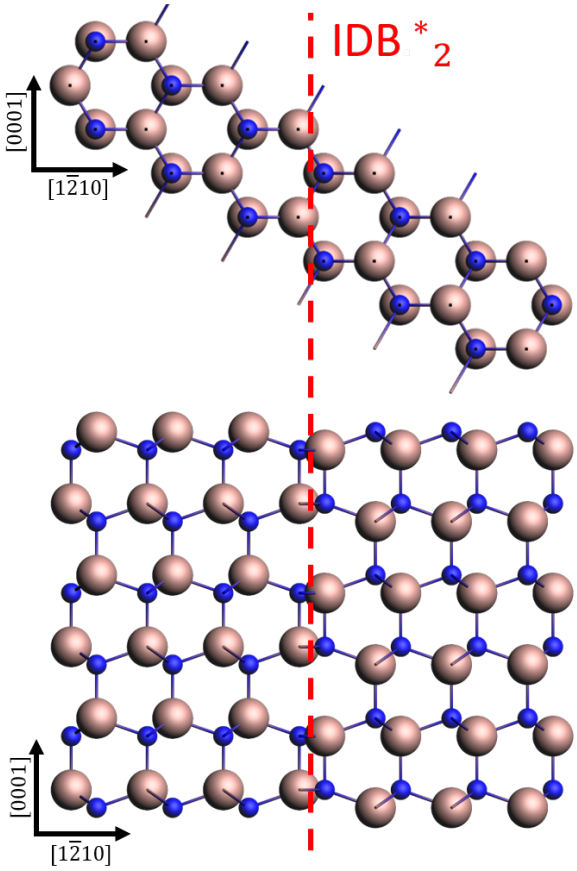

Figure 3.4: (0001)-planar (top) and ($\bar{1}2\bar{1}0$)-planar views of IDB*$_2$ model.

and coincide with outline of the wire surface. The white lines are restricted to half-integer multiples of 60° from the horizontal. The resolution of the phase reconstruction map is fairly limited and the assignment of plane orientation is somewhat open to interpretation. However, there clearly are IDB orientations, that are different from $\{10\bar{1}0\}$. These planes are annotated with white lines, indicating the presence of aIDBs. Our annotations for aIDBs are only found in phase reconstruction maps corresponding to the bottom and center of the wire. This would suggest aIDBs are formed during epitaxial growth, but eventually coalesce to the energetically cheaper IDBs.

From the results reported in table 3.6, PSFs, have one viable configuration. A similar analysis could be performed on $\{10\bar{1}0\}$-planar stacking mismatch boundaries (SMB).

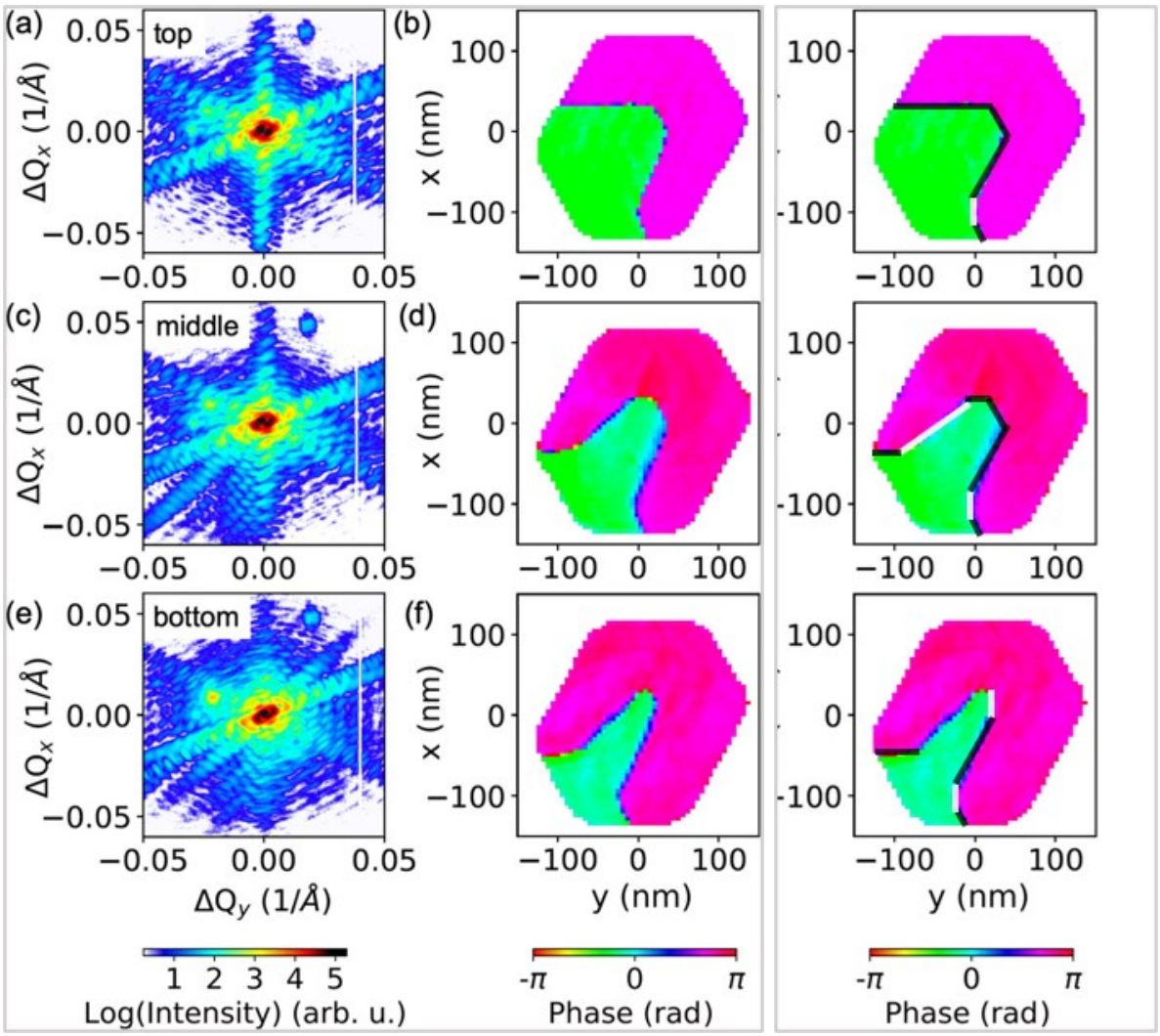

(A) (B)

Figure 3.5: (A) Bragg coherent X-ray diffraction measurements (images in left column) and corresponding real space reconstruction of the phase. Each row corresponds to measurements at different heights from the wire-substrate interface. Top, center, and bottom rows respectively correspond to measurements at the top, center, and bottom of the wire. (B) Interior boundaries annotated to as $\{10\bar{1}0\}$ (black) or $\{\bar{1}2\bar{1}0\}$ (white). [Reprinted (A) and adapted (B) with permission from [64]. Copyright 2020 American Chemical Society. *Original Caption : Coherent X-ray diffraction measurements of the 004 GaN Bragg peak (left) and their associated real space reconstruction of the phase (right) at the top (a, b), center (c, d), and bottom (e, f) of the 3.6 μm long wire B.)*]

Similar to PSFs, SMBs are expected to present with only one viable configuration, which can be denoted by,

$$\frac{\cdots \quad A \quad B \quad \cdots_{(+)}}{\cdots \quad A \quad B \quad \cdots_{(+)}} \ _{\{10\bar{1}0\}} \ . \tag{3.12}$$

Analyzing SMBs has significantly increased computational cost due to the possibility of type-1 and type-2 $\{10\bar{1}0\}$-planes. Another reason for the increased computational cost is SMB models require defect supercells that contain six defect planes to maintain periodicity (see sec. 3 and last paragraph of sec. 2.3.1 for further details). Additionally, SMBs are not expected to persist during epigrowth, due to the possibility of an SMB being terminated by a stacking fault [33]. For these reasons we have not performed extensive analysis on SMB models in wurtzites.

Chapter 4

Conclusions and Outlook.

The research presented in this dissertation has been centered around proposing alternative models for inversion domain boundaries in wurtzite materials. Our investigations are greatly aided by the notation schema that we introduce. Recall the notation,

$$\frac{\cdots \quad A \quad B \quad \cdots_{(+)}}{\cdots \quad \alpha \quad \beta \quad \cdots_{sign(u)}} \quad \cdots\{hklm\}, \tag{4.1}$$

specifies the mismatch in stacking sequence and polarity between the domains and the orientation of the separating plane. Depending on the values of $sign(u)$ and $\{hklm\}$ the notation can be used to characterize IDBs, aIDBs, PSFs, and SMBs as shown in table 3.1. The different possibilities for the stacking sequence mismatch (determined by the values of α and β) correspond to the possible models for each defect category.

For the $\{10\bar{1}0\}$-planar IDBs ($\{hklm\} = \{10\bar{1}0\}$ and $u < 0$), with appropriately chosen values for α and β we can denote the previously existing IDB defect models IDB* and Holt-IDB. Enumerating the alternative possible values for α and β yielded

two alternative models for IDBs, which we labelled IDB′ and IDB″. Ab-initio DFT calculations reveal that the newly proposed IDB′ model is energetically viable in all materials studied while IDB″ is universally unviable.

Similarly we study possible models for $\{\bar{1}2\bar{1}0\}$-planar inversion domain boundaries, prismatic stacking faults, and stacking mismatch boundaries. For aIDBs, we proposed two models - aIDB* and aIDB′. The only viable models resulting from the same analysis for PSFs and SMBs are the models already discussed in existing literature.

Here, we revisit the motivations for proposing new models for inversion domain boundaries, stated in sec. 1.3. One of the motivations is to better understand the atomic configuration arising from the intersection of IDBs with stacking faults. As discussed in sec. 2.4, IDB′ is the most suitable model to explain the transformation of IDB* when intersected by an I_1 stacking fault. Prior to this finding, the transformed defect plane has been misidentified as the Holt-IDB, presumably due to the lack of knowledge about IDB′. Further, in sec. 2.4, we show that extending our notation allows for the analysis of intersection of IDB* (and by extension other IDB models) with different types of stacking faults. Furthermore, as mentioned in sec. 1.3, understanding domain wall motion, is facilitated by expanding the list of viable models for IDBs.

Another motivation for introducing new models for IDBs is to understand the mechanisms behind domain wall motion. As shown in sec. 3.5 (see fig. 3.5 and accompanying discussion), the (0001)-planar cross section of polarity inverted domains within GaN nanowires evolve with wire growth. We show that, in some cases, the separating plane between the polarity inverted domains corresponds to the $\{\bar{1}2\bar{1}0\}$ orientation, indicating the presence of aIDBs. However, we have not found any previous discussions on aIDBs in the literature. The aIDB* and aIDB′ models that we propose are suitable candidates

to explain the observed aIDBs.

The newly proposed models presented in this dissertation are not sufficient to entirely explain inversion domain wall motion. Domain wall motion requires the presence of inversion domain boundaries in the basal plane or pyramidal planes. Here basal plane refers to the (0001) plane, and pyramidal planes refer to any plane $\{hklm\}$, such that $m \neq 0$ and h, k, and l are not all equal to zero. Examples of discussions on basal planar IDBs with [83, 84] or without [85–87] impurity atoms at the interface, and pyramidal planar IDBs with impurity atoms at the interface [88–90] can be found elsewhere. This dissertation does not contain discussion on basal planar or pyramidal planar inversion domain boundaries, since they are cannot be treated with our defect notation. Nevertheless, from the existing studies on these defects, we can identify possible questions for future investigations. One such area of investigation would be the effects of inclusion of impurity atoms along prismatic planar ($\{10\bar{1}0\}$ or $\{\bar{1}2\bar{1}0\}$) inversion domain boundaries. Another potential topic of interest would be an attempt to propose models for pyramidal planar IDBs that do not require the presence of impurity atoms.

In sec. 2.4 we discuss the sensitivity, of the IDB* model in GaN, to picometer scale inter-domain shifts (δz) to the initial configuration. Here, δz is the difference between the **c**-axis coordinate of a Ga atom basal plane in the Ga-polar domain and the corresponding N atomic plane in the N-polar domain. Using DFT analysis, Lançon et al. [80] show that the optimal configuration for IDB* in GaN is obtained when an initial inter-domain shift greater than 3.1 pm is introduced (i.e. $\delta z_{initial} > 3.1$ pm); the relaxed inter-domain shift for such an initial configuration is $\delta z_{relaxed} = 8$ pm. δz measurements at different heights from the substrate in multiple GaN nanowires are reported in [64]. At the top of the wires the reported δz values (8.3 ± 1.0 pm, 7.5 ± 1.0 pm, and 6.0 ± 1.0 pm) indicate δz converges to the $\delta z_{relaxed} = 8$ pm corresponding to the modified IDB* model proposed by Lançon

et al. Measurements of δz at the bottom of the wires (10.8 ± 1.0 pm, 8.8 ± 1.0 pm, and 11.5 ± 1.0 pm) do not all agree with the $\delta z_{relaxed} = 8$ pm of the IDB* model, indicating the possible presence of different IDB models at the initial stages of wire growth. Further calculations are required to determine the optimal relaxed $\delta z_{relaxed}$ values for the IDB models we propose in this dissertation. The results of such calculations could provide further confirmation of the existence of these models in real world samples.

Additionally, further study is required to analyze the electronic signatures of the defect models proposed in this dissertation. Our DFT calculations are performed using PBE functionals; which produce accurate results for structure relaxation. However, these functionals are not suitable for analyzing band structures due to their well documented tendency of under estimating band gaps [91]. Accurate characterization of changes to band structure - induced by the models proposed here - can be achieved by performing DFT calculations employing hybrid functionals.

Appendix

Further Details on Density Functional Theory Calculations.

1 Introduction.

Ab-initio density functional theory (DFT) calculations have been the instrumental in our search for new models for planar defects in wurtzites. For the defect models that we propose we evaluate associated domain wall energies and infer energetic viability using DFT. When performing DFT calculations there are a few choices that need to be made in terms of computational parameters. The choice of parameters impacts the computational time cost, accuracy and uncertainty of results of results, and eliminations of sources of error. DFT results are by definition approximations of physical reality. As such, careful consideration of the computational parameters is a key undertaking of DFT practitioners; to balance the desire for increased accuracy and confidence results with expense of computational resources.

According (2.17) the calculation domain wall energy of defect planes - involves the difference in total energy of two systems: the defect supercell and a pristine supercell with equal number of atoms. The chosen computational parameters must be consistent between the two total energy calculations for these supercells, to avoid computational artifacts in the result. Further, meaningful comparison between domain wall energies of the various defect models also requires consistency of computational parameters across all of the DFT calculations.

In the following we present and justify the choices we made regarding computational parameters and explain our reasoning. Our DFT calculations were performed using Vienna Ab-initio Simulation Package (VASP) [74, 75]. Exchange correlation effects were treated using the Perdew-Burke-Ernzerhof (PBE) functional [76] under the generalized gradient approximation. Pseudopotentials for the the treatment of core [77,78] states were chosen from the project augmented wave (PAW) potentials shipped with the VASP code base. The PAW potentials recommended by VASP for use with the PBE functional were used. Listed in table .1 are the recommended PAW potentials, default cutoff (ENMAX), valency, and valence electron configurations for the elements making up the wurtzite materials we studied.

Apart from choosing the the appropriate PAW potential, there are two more important choices in the setup of DFT calculations. The first parameter is the cutoff energy (E_{cut}), which specifies the cutoff energy for the plane-wave-basis set used to describe the electron density and orbitals of the system. The second important choice is the grid of k-point values used to sample the Brillouin zone in the reciprocal space. Apart from these parameter choices in the setup phase, an important aspect to consider is convergence of domain wall energies with respect to defect plane separation in the defect supercells. Supercells containing defect planes need to contain multiple instances of

Table .1: Pseudopotential files and associated valence electron configurations for compositional elements of the materials studied.

Element	Pseudopotential Name	ENMAX (eV)	Valency	Valence Electron configuration
Al	Al	240	3	$3s^2\ 3p^1$
B	B	319	3	$2s^2\ 2p^1$
Ga	Ga_d	283	13	$3d^{10}\ 4s^2\ 4p^1$
Zn	Zn	277	12	$3d^{10}\ 4p^2$
N	N	400	5	$2s^2\ 2p^3$
O	O	400	6	$2s^2\ 2p^4$
S	S	259	6	$3s^2\ 3p^4$

the defect plane to recover periodicity. To avoid spurious interactions between defect planes, defect supercells need to be sufficiently large to allow enough separation between the contained defect planes and their periodic repetitions; since we are interested in domain wall energies of defects in real samples where there is no constraint requiring the formation of another defect plane close by. Similarly, when determining the surface energies of the prismatic planes of interest the thickness of the vacuum region needs to be sufficiently large to minimize interactions between the periodically repeated slabs. In the final section of this appendix we discuss the creation of supercells (mentioned in sec. 2.3) that require the inclusion of six defect planes to recover periodicity.

2 Choice of computational parameters

2.1 Cutoff Energy

The PAW potentials used in our DFT calculations are designed to work reliably with E_{cut} of 250 eV to make calculations computationally cheap. Increased accuracy can be achieved by increasing E_{cut}. The default cutoff for calculations is set by the *ENMAX* tag in the POTCAR file. The default cutoff can be overridden (it is generally recommended to do so) by specifying an *ENCUT* tag in the INCAR file.

Our methodology for choosing the optimal E_{cut} has evolved over the course of our research. For the results presented in chap. 2, E_{cut} was chosen such that the total energy of the primitive unit cell was to 1 m eV. In GaN, this requirement corresponded to $E_{cut} = 900$ eV; see fig. .1(a) for the plot of the total energy of a GaN primitive unit cell vs E_{cut}. However, the goal of our calculations is to evaluate domain wall energy to an accuracy of 1 m eV/Å^2. Since domain wall energy is calculated using the difference in total energy between two supercells, the accuracy of domain wall energy converges to the desired accuracy of 1 m eV/Å^2 with a lower E_{cut} (see fig. .1(c) showing the convergence of super energy of the IDB* defect with respect E_{cut}) even if the total energies of the individual supercells used to calculate Γ do not converge for this E_{cut} - as can be seen from fig. .1(b). Note the scale of the y-axis in the Γ_{IDB*} vs cutoff energy plot in fig. .1(c) shows that the fluctuations in Γ_{IDB*} values with respect to the different cutoff energies tested is well within the target accuracy. Hence, we are free to choose a cutoff energy within the range cutoff energy values tested here; favoring lower cutoff energies helps the computational cost down.

Ultimately, for GaN we chose an E_{cut}520 eV, which is equal to 1.3× the largest

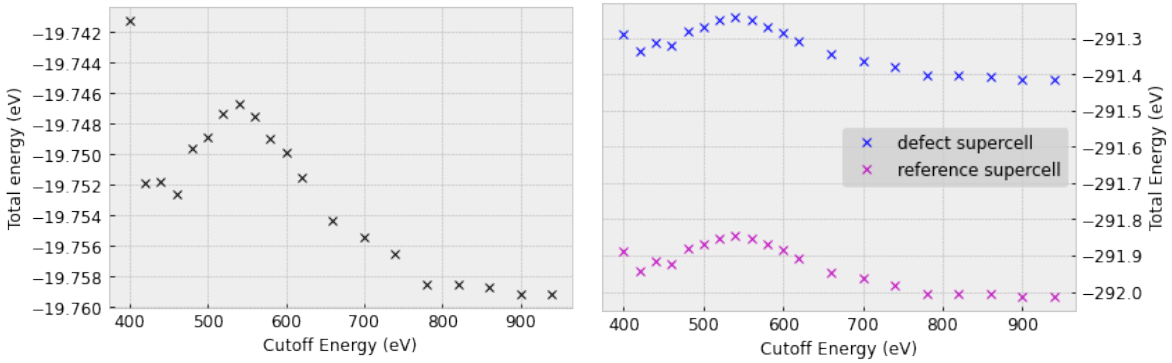

(a) (b)

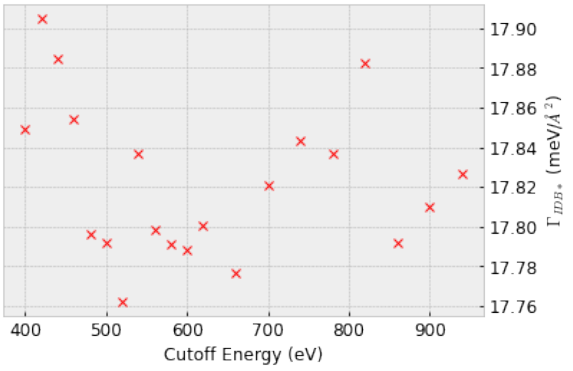

(c)

Figure .1: (a) GaN primitive unit cell total energy vs cutoff energy
(b) Total energy vs cutoff energy for IDB* defect supercell ($12 \times 1 \times 1$ defect supercell containing two IDB* defect planes) and reference supercell (pristine supercell of same size and number of atoms as defect supercell).
(c) Γ_{IDB*} (y-axis on the left) and ΔE (total energy difference between defect and reference supercells, y-axis on the right) vs cutoff energy.

ENMAX from the POTCAR file; this is the default E_{cut} set by VASP when the INCAR tag *PREC* is set to 'Accurate' and the *ENCUT* tag is not set. Similarly, for each of the wurtzite materials studied we used $E_{cut} = 1.3\times$ (largest *ENMAX*) from the POTCAR file corresponding to each material. Table 3.2 lists resulting choices for E_{cut} for each material.

2.2 Sampling of reciprocal (k-)space.

The number of k-points used sample the Brillouin zone were specified using the KPOINTS input file. The KPOINTS file automatically generates the Gamma-centered grid points based on the specified number of points ($n(k_i)$) along each reciprocal lattice vector ($\mathbf{b}_i$). Here, the mesh being Gamma-centered is important to preserve the hexagonal symmetry

of the wurtzite structure.

Our calculations used supercells of different sizes resulting in the requirement to choose different $n(k_i)$ values for each supercell. The $n(k_i)$ values were chosen to allow a certain maximum k-point separation. The procedure for determining the maximum allowed k-point separation ($\max(\mathrm{k}_{sep})$) for a given material was as follows.

- The set of $n(k_i)$ values that converges the total energy of a primitive unit cell to 1 m eV was determined manually.

- The maximum ratio of $\frac{\mathbf{b}_i}{n(k_i)}$, rounded down to the nearest integer multiple of 0.05Å^{-1} for convenience, was chosen as $\max(\mathrm{k}_{sep})$.

From the chosen maximum k-point separation, the $n(k_i)$ values for a given supercell determined as the ratio of supercell reciprocal lattice vector to $\max(\mathrm{k}_{sep})$ rounded up to an integer.

3 Defect supercells requiring the inclusion of of six defect planes.

In sec. 2.3 we discuss the need to create defect supercells containing six defect planes to recover periodicity when estimating domain wall energy of the IDB′ and IDB″ defects (see fig. 2.5 and accompanying discussion). Here we provide fig. Appx.2 illustrating the supercell created for the IDB′ defect in GaN.

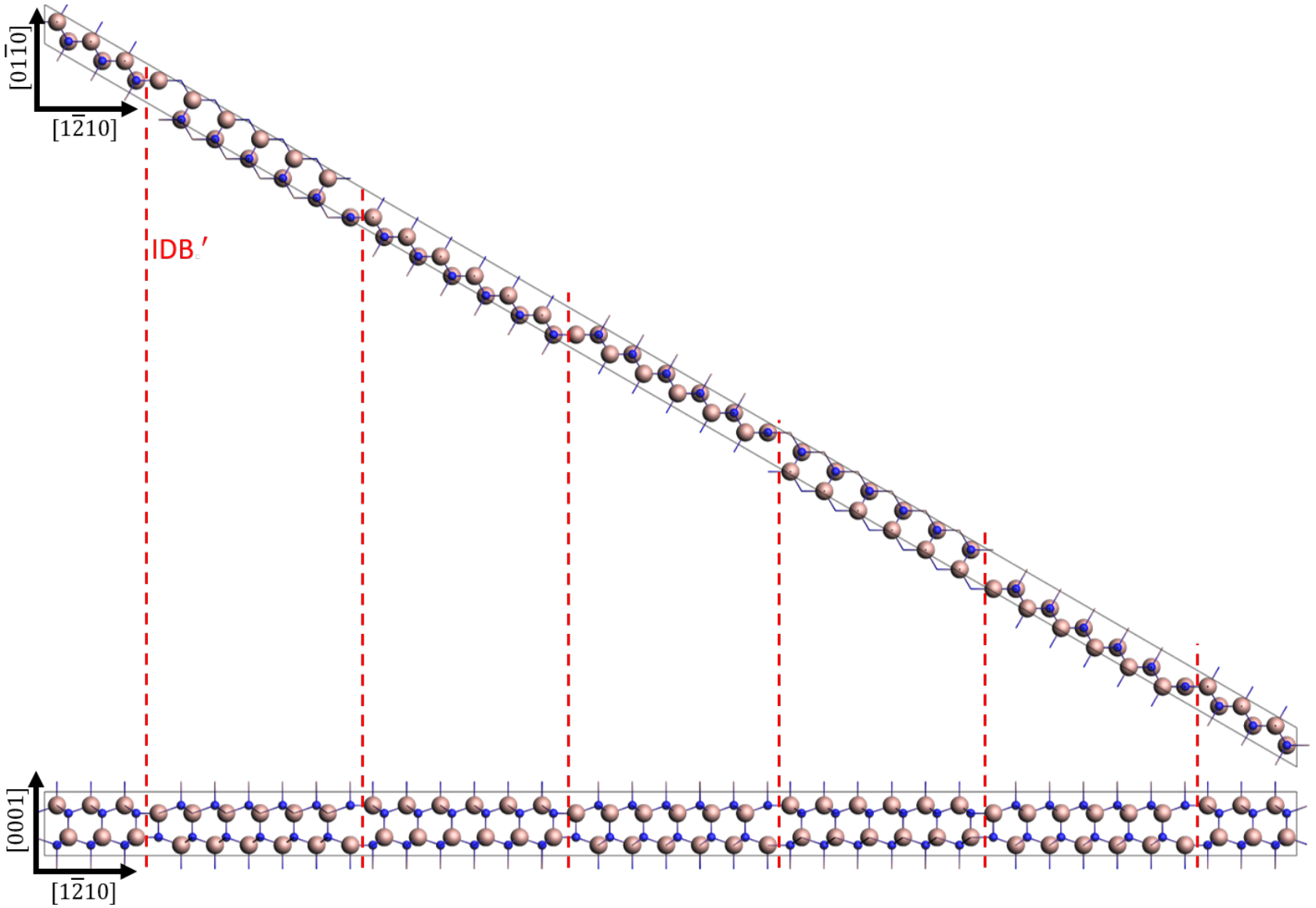

Figure .2: (0001)-planar (top) and (1$\bar{2}$10) planar (bottom) views of the supercell used to determine domain wall energy of IDB′ in GaN

Bibliography

[1] Vogel, D., P. Krüger, and J. Pollmann (1997) "Structural and Electronic Properties of Group-III Nitrides," *Physical Review B*, **55**(19), pp. 12836–12839.

[2] Gavrilenko, V. I. and R. Q. Wu (2000) "Linear and Nonlinear Optical Properties of Group-III Nitrides," *Physical Review B*, **61**(4), pp. 2632–2642.

[3] Nakamura, S., M. Senoh, S.-i. Nagahama, N. Iwasa, T. Yamada, T. Matsushita, H. K. H. Kiyoku, and Y. S. Y. Sugimoto (1996) "InGaN-Based Multi-Quantum-Well-Structure Laser Diodes," *Japanese Journal of Applied Physics*, **35**(1B), p. L74.

[4] Akasaki, I. (2015) "Nobel Lecture: Fascinated Journeys into Blue Light," *Reviews of Modern Physics*, **87**(4), pp. 1119–1131.

[5] Li, D., K. Jiang, X. Sun, and C. Guo (2018) "AlGaN Photonics: Recent Advances in Materials and Ultraviolet Devices," *Advances in Optics and Photonics*, **10**(1), pp. 43–110.

[6] Armstrong, A. M., B. A. Klein, A. A. Allerman, A. G. Baca, M. H. Crawford, J. Podkaminer, C. R. Perez, M. P. Siegal, E. A. Douglas, V. M. Abate, and F. Leonard (2019) "Visible- and Solar-Blind Photodetectors Using AlGaN High Electron Mobility Transistors with a Nanodot-Based Floating Gate," *Photonics Research*, **7**(6), pp. B24–B31.

[7] Amano, H., Y. Baines, E. Beam, M. Borga, T. Bouchet, P. R. Chalker, M. Charles, K. J. Chen, N. Chowdhury, R. Chu, C. D. Santi, M. M. D. Souza, S. Decoutere, L. D. Cioccio, B. Eckardt, T. Egawa, P. Fay, J. J. Freedsman, L. Guido, O. Häberlen, G. Haynes, T. Heckel, D. Hemakumara, P. Houston, J. Hu, M. Hua, Q. Huang, A. Huang, S. Jiang, H. Kawai,

D. Kinzer, M. Kuball, A. Kumar, K. B. Lee, X. Li, D. Marcon, M. März, R. McCarthy, G. Meneghesso, M. Meneghini, E. Morvan, A. Nakajima, E. M. S. Narayanan, S. Oliver, T. Palacios, D. Piedra, M. Plissonnier, R. Reddy, M. Sun, I. Thayne, A. Torres, N. Trivellin, V. Unni, M. J. Uren, M. V. Hove, D. J. Wallis, J. Wang, J. Xie, S. Yagi, S. Yang, C. Youtsey, R. Yu, E. Zanoni, S. Zeltner, and Y. Zhang (2018) "The 2018 GaN Power Electronics Roadmap," *Journal of Physics D: Applied Physics*, **51**(16), p. 163001.

[8] Meneghesso, G., G. Verzellesi, F. Danesin, F. Rampazzo, F. Zanon, A. Tazzoli, M. Meneghini, and E. Zanoni (2008) "Reliability of GaN High-Electron-Mobility Transistors: State of the Art and Perspectives," *IEEE Transactions on Device and Materials Reliability*, **8**(2), pp. 332–343.

[9] Zhou, B., X. Kong, S. Vanka, S. Cheng, N. Pant, S. Chu, P. Ghamari, Y. Wang, G. Botton, H. Cuo, and Z. Mi (2019) "A GaN:Sn Nanoarchitecture Integrated on a Silicon Platform for Converting CO 2 to HCOOH by Photoelectrocatalysis," *Energy & Environmental Science*, **12**(9), pp. 2842–2848.

[10] Emani, N. K., E. Khaidarov, R. Paniagua-Domínguez, Y. H. Fu, V. Valuckas, S. Lu, X. Zhang, S. T. Tan, H. V. Demir, and A. I. Kuznetsov (2017) "High-Efficiency and Low-Loss Gallium Nitride Dielectric Metasurfaces for Nanophotonics at Visible Wavelengths," *Applied Physics Letters*, **111**(22), p. 221101.

[11] Hoo Teo, K., Y. Zhang, N. Chowdhury, S. Rakheja, R. Ma, Q. Xie, E. Yagyu, K. Yamanaka, K. Li, and T. Palacios (2021) "Emerging GaN Technologies for Power, RF, Digital, and Quantum Computing Applications: Recent Advances and Prospects," *Journal of Applied Physics*, **130**(16), p. 160902.

[12] Lester, S. D., F. A. Ponce, M. G. Craford, and D. A. Steigerwald (1995) "High Dislocation Densities in High Efficiency GaN-based Light-emitting Diodes," *Applied Physics Letters*, **66**(10), pp. 1249–1251.

[13] Deb, P., H. Kim, V. Rawat, M. Oliver, S. Kim, M. Marshall, E. Stach, and T. Sands (2005) "Faceted and Vertically Aligned GaN Nanorod Arrays Fabricated without Catalysts or Lithography," *Nano Letters*, **5**(9), pp. 1847–1851.

[14] Hersee, S. D., X. Sun, and X. Wang (2006) "The Controlled Growth of GaN Nanowires," *Nano Letters*, **6**(8), pp. 1808–1811.

[15] Chen, X. J., G. Perillat-Merceroz, D. Sam-Giao, C. Durand, and J. Eymery (2010) "Homoepitaxial Growth of Catalyst-Free GaN Wires on N-polar Substrates," *Applied Physics Letters*, **97**(15), p. 151909.

[16] Kim, W., Ö. Aktas, A. E. Botchkarev, A. Salvador, S. N. Mohammad, and H. Morkoç (1996) "Reactive Molecular Beam Epitaxy of Wurtzite GaN: Materials Characteristics and Growth Kinetics," *Journal of Applied Physics*, **79**(10), pp. 7657–7666.

[17] Sekiguchi, H., K. Kishino, and A. Kikuchi (2008) "Ti-Mask Selective-Area Growth of GaN by RF-Plasma-Assisted Molecular-Beam Epitaxy for Fabricating Regularly Arranged InGaN/GaN Nanocolumns," *Applied Physics Express*, **1**(12), p. 124002.

[18] Bengoechea-Encabo, A., F. Barbagini, S. Fernandez-Garrido, J. Grandal, J. Ristic, M. A. Sanchez-Garcia, E. Calleja, U. Jahn, E. Luna, and A. Trampert (2011) "Understanding the Selective Area Growth of GaN Nanocolumns by MBE Using Ti Nanomasks," *Journal of Crystal Growth*, **325**(1), pp. 89–92.

[19] Geelhaar, L., C. Chèze, B. Jenichen, O. Brandt, C. Pfüller, S. Münch, R. Rothemund, S. Reitzenstein, A. Forchel, T. Kehagias, P. Komninou, G. P. Dimitrakopulos, T. Karakostas, L. Lari, P. R. Chalker, M. H. Gass, and H. Riechert (2011) "Properties of GaN Nanowires Grown by Molecular Beam Epitaxy," *IEEE Journal of Selected Topics in Quantum Electronics*, **17**(4), pp. 878–888.

[20] Sverdlov, B. N., G. A. Martin, H. Morkoç, and D. J. Smith (1995) "Formation of Threading Defects in GaN Wurtzite Films Grown on Nonisomorphic Substrates," *Applied Physics Letters*, **67**(14), pp. 2063–2065.

[21] Smith, D. J., D. Chandrasekhar, B. Sverdlov, A. Botchkarev, A. Salvador, and H. Morkoç (1995) "Characterization of Structural Defects in Wurtzite GaN Grown on 6H SiC Using Plasma-enhanced Molecular Beam Epitaxy," *Applied Physics Letters*, **67**(13), pp. 1830–1832.

[22] Ren, S. Y. and J. D. Dow (1996) "Lattice-matching SiC Substrates with GaN," *Applied Physics Letters*, **69**(2), pp. 251–253.

[23] Kuramata, A., K. Horino, K. Domen, K. Shinohara, and T. Tanahashi

(1995) "High-quality GaN Epitaxial Layer Grown by Metalorganic Vapor Phase Epitaxy on (111) MgAl2O4 Substrate," *Applied Physics Letters*, **67**(17), pp. 2521–2523.

[24] Watanabe, A., T. Takeuchi, K. Hirosawa, H. Amano, K. Hiramatsu, and I. Akasaki (1993) "The Growth of Single Crystalline GaN on a Si Substrate Using AIN as an Intermediate Layer," *Journal of Crystal Growth*, **128**(1), pp. 391–396.

[25] Fujieda, S. F. S. and Y. M. Y. Matsumoto (1991) "Structure Control of GaN Films Grown on (001) GaAs Substrates by GaAs Surface Pretreatments," *Japanese Journal of Applied Physics*, **30**(9B), p. L1665.

[26] Hamdani, F., A. Botchkarev, W. Kim, H. Morkoç, M. Yeadon, J. M. Gibson, S.-C. Y. Tsen, D. J. Smith, D. C. Reynolds, D. C. Look, K. Evans, C. W. Litton, W. C. Mitchel, and P. Hemenger (1997) "Optical Properties of GaN Grown on ZnO by Reactive Molecular Beam Epitaxy," *Applied Physics Letters*, **70**(4), pp. 467–469.

[27] Liu, M.-C., Y.-J. Cheng, J.-R. Chang, S.-C. Hsu, and C.-Y. Chang (2011) "Optical Properties of Self Assembled GaN Polarity Inversion Domain Boundary," *Applied Physics Letters*, **99**(2), p. 021103.

[28] Kong, X., H. Li, S. Albert, A. Bengoechea-Encabo, M. A. Sanchez-Garcia, E. Calleja, C. Draxl, and A. Trampert (2016) "Titanium Induced Polarity Inversion in Ordered (In,Ga)N/GaN Nanocolumns," *Nanotechnology*, **27**(6), p. 065705.

[29] Xiao, P., X. Wang, J. Wang, F. Ke, M. Zhou, and Y. Bai (2009) "Surface Transformation and Inversion Domain Boundaries in Gallium Nitride Nanorods," *Applied Physics Letters*, **95**(21), p. 211907.

[30] Zhang, J. Y., Y. P. Xie, H. B. Guo, and Y. G. Chen (2018) "Thermodynamics of Inversion-Domain Boundaries in Aluminum Nitride: Interplay between Interface Energy and Electric Dipole Potential Energy," *Journal of Applied Physics*, **123**(17), p. 175301.

[31] Sitar, Z., M. J. Paisley, B. Yan, and R. F. Davis (1989/ed) "Structural Defects in GaN Epilayers Grown by Gas Source Molecular Beam Epitaxy," *MRS Online Proceedings Library Archive*, **162**.

[32] Yeadon, M., F. Hamdani, G. Y. Xu, A. Salvador, A. E. Botchkarev, J. M. Gibson, and H. Morkoç (1997) "Surface Morphology and Optical Characterization of GaN Grown on α-Al2O3 (0001) by Radio-Frequency-Assisted Molecular Beam Epitaxy," *Applied Physics Letters*, **70**(22), pp. 3023–3025.

[33] Northrup, J. E., J. Neugebauer, and L. T. Romano (1996) "Inversion Domain and Stacking Mismatch Boundaries in GaN," *Physical Review Letters*, **77**(1), pp. 103–106.

[34] Hellman, E. S. (1998/ed) "The Polarity of GaN: A Critical Review," *Materials Research Society Internet Journal of Nitride Semiconductor Research*, **3**.

[35] Stutzmann, M., O. Ambacher, M. Eickhoff, U. Karrer, A. Lima Pimenta, R. Neuberger, J. Schalwig, R. Dimitrov, P. Schuck, and R. Grober (2001) "Playing with Polarity," *physica status solidi (b)*, **228**(2), pp. 505–512.

[36] Bykhovski, A., B. Gelmont, and M. Shur (1993) "The Influence of the Strain-induced Electric Field on the Charge Distribution in GaN-AlN-GaN Structure," *Journal of Applied Physics*, **74**(11), pp. 6734–6739.

[37] Seelmann-Eggebert, M., J. L. Weyher, H. Obloh, H. Zimmermann, A. Rar, and S. Porowski (1997) "Polarity of (00.1) GaN Epilayers Grown on a (00.1) Sapphire," *Applied Physics Letters*, **71**(18), pp. 2635–2637.

[38] Martin, G., A. Botchkarev, A. Rockett, and H. Morkoç (1996) "Valence-band Discontinuities of Wurtzite GaN, AlN, and InN Heterojunctions Measured by X-ray Photoemission Spectroscopy," *Applied Physics Letters*, **68**(18), pp. 2541–2543.

[39] Kirilyuk, V., A. R. A. Zauner, P. C. M. Christianen, J. L. Weyher, P. R. Hageman, and P. K. Larsen (2000) "Exciton-Related Photoluminescence in Homoepitaxial GaN of Ga and N Polarities," *Applied Physics Letters*, **76**(17), pp. 2355–2357.

[40] Chichibu, S. F., A. Setoguchi, A. Uedono, K. Yoshimura, and M. Sumiya (2001) "Impact of Growth Polar Direction on the Optical Properties of GaN Grown by Metalorganic Vapor Phase Epitaxy," *Applied Physics Letters*, **78**(1), pp. 28–30.

[41] Karrer, U., O. Ambacher, and M. Stutzmann (2000) "Influence of Crystal Polarity on the Properties of Pt/GaN Schottky Diodes," *Applied Physics Letters*, **77**(13), pp. 2012–2014.

[42] Sumiya, M., K. Yoshimura, K. Ohtsuka, and S. Fuke (2000) "Dependence of Impurity Incorporation on the Polar Direction of GaN Film Growth," *Applied Physics Letters*, **76**(15), pp. 2098–2100.

[43] Li, S. F., S. Fuendling, X. Wang, S. Merzsch, M. A. M. Al-Suleiman, J. D. Wei, H.-H. Wehmann, A. Waag, W. Bergbauer, and M. Strassburg (2011) "Polarity and Its Influence on Growth Mechanism during MOVPE Growth of GaN Sub-micrometer Rods," *Crystal Growth & Design*, **11**(5), pp. 1573–1577.

[44] Aminoff, G. and B. Broomé (1931) "Strukturtheoretische Studien über Zwillinge. I." *Zeitschrift für Kristallographie - Crystalline Materials*, **80**(1-6), pp. 355–376.

[45] Holt, D. B. (1969) "Antiphase Boundaries in Semiconducting Compounds," *Journal of Physics and Chemistry of Solids*, **30**(6), pp. 1297–1308.

[46] Ruterana, P. and G. Nouet (2001) "Atomic Structure of Extended Defects in Wurtzite GaN Epitaxial Layers," *physica status solidi (b)*, **227**(1), pp. 177–228.

[47] Potin, V., G. Nouet, and P. Ruterana (1999) "Evidence for Multiple Atomic Structure for the $\{10\bar{1}0\}$ Inversion Domain Boundaries in GaN Layers," *Applied Physics Letters*, **74**(7), pp. 947–949.

[48] Austerman, S. B. and W. G. Gehman (1966) "The Inversion Twin: Prototype in Beryllium Oxide," *Journal of Materials Science*, **1**(3), pp. 249–260.

[49] Cherns, D., W. T. Young, M. Sanders, J. W. Steeds, F. A. Ponce, and S. Nakamura (1998) "Determination of the Atomic Structure of Inversion Domain Boundaries in α-GaN by Transmission Electron Microscopy," *Philosophical Magazine A*, **77**(1), pp. 273–286.

[50] Romano, L. T., J. E. Northrup, and M. A. O'Keefe (1996) "Inversion Domains in GaN Grown on Sapphire," *Applied Physics Letters*, **69**(16), pp. 2394–2396.

[51] Auzelle, T., B. Haas, M. D. Hertog, J.-L. Rouvière, B. Daudin, and B. Gayral (2015) "Attribution of the 3.45 eV GaN Nanowires Luminescence to Inversion Domain Boundaries," *Applied Physics Letters*, **107**(5), p. 051904.

[52] Lähnemann, J., U. Jahn, O. Brandt, T. Flissikowski, P. Dogan, and H. T. Grahn (2014) "Luminescence Associated with Stacking Faults in GaN," *ResearchGate*.

[53] Fiorentini, V. (2003) "Origin of the Efficient Light Emission from Inversion Domain Boundaries in GaN," *Applied Physics Letters*, **82**(8), pp. 1182–1184.

[54] Wu, C. H., P. Y. Lee, K. Y. Chen, Y. T. Tseng, Y. L. Wang, and K. Y. Cheng (2016) "Selective Area Growth of High-Density GaN Nanowire Arrays on Si(111) Using Thin AlN Seeding Layers," *Journal of Crystal Growth*, **454**, pp. 71–81.

[55] Aseev, P., Ž. Gačević, A. Torres-Pardo, J. M. González-Calbet, and E. Calleja (2016) "Improving Optical Performance of GaN Nanowires Grown by Selective Area Growth Homoepitaxy: Influence of Substrate and Nanowire Dimensions," *Applied Physics Letters*, **108**(25), p. 253109.

[56] Brubaker, M. D., S. M. Duff, T. E. Harvey, P. T. Blanchard, A. Roshko, A. W. Sanders, N. A. Sanford, and K. A. Bertness (2016) "Polarity-Controlled GaN/AlN Nucleation Layers for Selective-Area Growth of GaN Nanowire Arrays on Si(111) Substrates by Molecular Beam Epitaxy," *Crystal Growth & Design*, **16**(2), pp. 596–604.

[57] Mitrofanov, M. I., I. V. Levitskii, G. V. Voznyuk, E. E. Tatarinov, S. N. Rodin, M. A. Kaliteevski, and V. P. Evtikhiev (2018) "Concentric Hexagonal GaN Structures for Nanophotonics, Fabricated by Selective Vapor-Phase Epitaxy with Ion-Beam Etching," *Semiconductors*, **52**(7), pp. 954–956.

[58] Sobanska, M., Z. R. Zytkiewicz, K. Klosek, R. Kruszka, K. Golaszewska, M. Ekielski, and S. Gieraltowska (2020) "Selective Area Formation of GaN Nanowires on GaN Substrates by the Use of Amorphous Al_xO_y Nucleation Layer," *Nanotechnology*, **31**(18), p. 184001.

[59] Sanchez, A. M., G. Nouet, P. Ruterana, F. J. Pacheco, S. I. Molina, and R. Garcia (2001) "A Mechanism for the Multiple Atomic Configurations of Inversion Domain Boundaries in GaN Layers Grown on Si(111)," *Applied Physics Letters*, **79**(22), pp. 3588–3590.

[60] Kioseoglou, J., P. Komninou, G. P. Dimitrakopulos, T. Kehagias, H. M. Polatoglou, G. Nouet, and T. Karakostas (2003) "Microstructure of Planar Defects and Their Interactions in Wurtzite GaN Films," *Solid-State Electronics*, **47**(3), pp. 553–557.

[61] Dimitrakopulos, G. P., P. Komninou, J. Kioseoglou, T. Kehagias, E. Sarigiannidou, A. Georgakilas, G. Nouet, and T. Karakostas (2001) "Struc-

tural Transition of Inversion Domain Boundaries through Interactions with Stacking Faults in Epitaxial GaN," *Physical Review B*, **64**(24), p. 245325.

[62] Kioseoglou, J., P. Komninou, and T. Karakostas (2008) "Interatomic potential calculations of III(Al, In)–N planar defects with a III-species environment approach," *physica status solidi (b)*, **245**(6), pp. 1118–1124.

[63] Labat, S., M.-I. Richard, M. Dupraz, M. Gailhanou, G. Beutier, M. Verdier, F. Mastropietro, T. W. Cornelius, T. U. Schülli, J. Eymery, and O. Thomas (2015) "Inversion Domain Boundaries in GaN Wires Revealed by Coherent Bragg Imaging," *ACS Nano*, **9**(9), pp. 9210–9216.

[64] Li, N., S. Labat, S. J. Leake, M. Dupraz, J. Carnis, T. W. Cornelius, G. Beutier, M. Verdier, V. Favre-Nicolin, T. U. Schülli, O. Thomas, J. Eymery, and M.-I. Richard (2020) "Mapping Inversion Domain Boundaries along Single GaN Wires with Bragg Coherent X-ray Imaging," *ACS Nano*, **14**(8), pp. 10305–10312.

[65] Liu, Z., B. Liu, F. Ren, Y. Yin, S. Zhang, M. Liang, Z. Dou, Z. Liu, S. Yang, J. Yan, T. Wei, X. Yi, C. Wu, T. Guo, J. Wang, Y. Zhang, J. Li, and P. Gao (2022) "Atomic-Scale Mechanism of Spontaneous Polarity Inversion in AlN on Nonpolar Sapphire Substrate Grown by MOCVD," *Small*, **18**(16), p. 2200057.

[66] Ferri, K., S. Bachu, W. Zhu, M. Imperatore, J. Hayden, N. Alem, N. Giebink, S. Trolier-McKinstry, and J.-P. Maria (2021) "Ferroelectrics Everywhere: Ferroelectricity in Magnesium Substituted Zinc Oxide Thin Films," *Journal of Applied Physics*, **130**(4), p. 044101.

[67] Fichtner, S., N. Wolff, F. Lofink, L. Kienle, and B. Wagner (2019) "AlScN: A III-V Semiconductor Based Ferroelectric," *Journal of Applied Physics*, **125**(11), p. 114103.

[68] Wang, P., D. Wang, N. M. Vu, T. Chiang, J. T. Heron, and Z. Mi (2021) "Fully Epitaxial Ferroelectric ScAlN Grown by Molecular Beam Epitaxy," *Applied Physics Letters*, **118**(22), p. 223504.

[69] Umar, M. M. F. and J. O. Sofo (2021) "Inversion Domain Boundaries in Wurtzite GaN," *Physical Review B*, **103**(16), p. 165305.

[70] Xia, H., Q. Xia, and A. L. Ruoff (1993) "High-Pressure Structure of Gallium Nitride: Wurtzite-to-rocksalt Phase Transition," *Physical Review B*, **47**(19), pp. 12925–12928.

[71] Ueno, M., M. Yoshida, A. Onodera, O. Shimomura, and K. Takemura (1994) "Stability of the Wurtzite-Type Structure under High Pressure: GaN and InN," *Physical Review B*, **49**(1), pp. 14–21.

[72] Wright, A. F. (1997) "Basal-Plane Stacking Faults and Polymorphism in AlN, GaN, and InN," *Journal of Applied Physics*, **82**(10), pp. 5259–5261.

[73] Stampfl, C. and C. G. Van de Walle (1998) "Energetics and Electronic Structure of Stacking Faults in AlN, GaN, and InN," *Physical Review B*, **57**(24), pp. R15052–R15055.

[74] Kresse, G. and J. Furthmüller (1996) "Efficiency of Ab-Initio Total Energy Calculations for Metals and Semiconductors Using a Plane-Wave Basis Set," *Computational Materials Science*, **6**(1), pp. 15–50.

[75] ——— (1996) "Efficient Iterative Schemes for Ab Initio Total-Energy Calculations Using a Plane-Wave Basis Set," *Physical Review B*, **54**(16), pp. 11169–11186.

[76] Perdew, J. P., K. Burke, and M. Ernzerhof (1996) "Generalized Gradient Approximation Made Simple," *Physical Review Letters*, **77**(18), pp. 3865–3868.

[77] Blöchl, P. E. (1994) "Projector Augmented-Wave Method," *Physical Review B*, **50**(24), pp. 17953–17979.

[78] Kresse, G. and D. Joubert (1999) "From Ultrasoft Pseudopotentials to the Projector Augmented-Wave Method," *Physical Review B*, **59**(3), pp. 1758–1775.

[79] Monkhorst, H. and J. Pack (1976) "Special Points for Brillouin-Zone Integrations," *Physical Review B*, **13**(12), pp. 5188–5192.

[80] Lançon, F., L. Genovese, and J. Eymery (2018) "Towards Simulation at Picometer-Scale Resolution: Revisiting Inversion Domain Boundaries in GaN," *Physical Review B*, **98**(16), p. 165306.

[81] Northrup, J. E. (1998) "Theory of the (12_10) Prismatic Stacking Fault in GaN,"

Applied Physics Letters, **72**(18), pp. 2316–2318.

[82] Liu, F., R. Collazo, S. Mita, Z. Sitar, S. J. Pennycook, and G. Duscher (2008) "Direct Observation of Inversion Domain Boundaries of GaN on C-Sapphire at Sub-ångstrom Resolution," *Advanced Materials*, **20**(11), pp. 2162–2165.

[83] Northrup, J. E. (2003) "Magnesium Incorporation at (0001) Inversion Domain Boundaries in GaN," *Applied Physics Letters*, **82**(14), pp. 2278–2280.

[84] Liu, Z., R.-Z. Wang, L.-M. Liu, H. Yan, and W.-M. Lau (2014) "Si Doping at GaN Inversion Domain Boundaries: An Interfacial Polar Field for Electron and Hole Separation," *Journal of Materials Chemistry A*, **2**(25), pp. 9744–9750.

[85] Li, S., H. Lei, P.-M. Anglade, J. Chen, and P. Ruterana (2018) "Structural Stability and Electronic Properties of the (0 0 0 1) Inversion Domain Boundary in III-nitrides," *Computational Materials Science*, **154**, pp. 152–158.

[86] Li, S., H. Lei, Y. Wang, M. B. Ullah, J. Chen, V. Avrutin, Ü. Özgür, H. Morkoç, and P. Ruterana (2018) "Polarity Control within One Monolayer at ZnO/GaN Heterointerface: (0001) Plane Inversion Domain Boundary," *ACS Applied Materials & Interfaces*, **10**(43), pp. 37651–37660.

[87] Li, S., H. Lei, Z. Wang, J. Chen, and P. Ruterana (2018) "Energetic and Electronic Properties of (0001) Inversion Domain Boundaries in ZnO," *physica status solidi (b)*, **255**(4), p. 1700429.

[88] Romano, L. T., J. E. Northrup, A. J. Ptak, and T. H. Myers (2000) "Faceted Inversion Domain Boundary in GaN Films Doped with Mg," *Applied Physics Letters*, **77**(16), pp. 2479–2481.

[89] Niki, K., T. Akiyama, and T. Ito (2022) "An Ab Initio-Based Approach for the Formation of Pyramidal Inversion Domain Boundaries in Highly Mg-doped GaN," *Japanese Journal of Applied Physics*, **61**(5), p. 055503.

[90] Persson, A. R., A. Papamichail, V. Darakchieva, and P. O. Å. Persson (2022) "Mg Segregation at Inclined Facets of Pyramidal Inversion Domains in GaN:Mg," *Scientific Reports*, **12**(1), p. 17987.

[91] Perdew, J. P. (1985) "Density Functional Theory and the Band Gap Problem," *International Journal of Quantum Chemistry*, **28**(S19), pp. 497–523.

Vita

Mohamed Mauroof F. Umar

Education:

Ph. D. in Physics — Aug. 2014 - Dec. 2022
The Pennsylvania State University, State College, Pa

Bachelor of Science (Hons.) Physics Special — May. 2009 - Jan. 2014
University of Peradeniya, Peradeniya, Sri Lanka

Primary and Secondary Level Education — 1994 - 2007
St. Anthony's College, Kandy, Sri Lanka

Publications:

[1] Umar, M. M. F. and Sofo, J.O. (2021) "Inversion Domain Boundaries in Wurtzite GaN", *Physical Review B*, **103**(16) p. 165305.

Conferences:

[1] Umar, M. M. F. and Sofo, J.O. *"Inversion Domain Boundaries in Wurtzite GaN."*
Presentation at American Physical March Meeting 2022, March 2022

[2] Umar, M. M. F. and Sofo, J.O. *"Inversion Domain Boundaries in Wurtzite Gallium Nitride."*
Virtual poster presentation at Materials Day 2021, hosted by Materials Research University, Pennsylvania State University, Aug. 2021.

[3] Umar, M. M. F. and Sofo, J.O. *"Effective Conductivity of an Inhomogeneous Sample."*
Poster presentation at Materials Day 2018, hosted by Materials Research University, Pennsylvania State University, Aug. 2018.

[4] Umar, M. M. F. and Sofo, J.O. *"Interface Energies in GaN nanostructures.;"*
Poster presentation at Materials Day 2017, hosted by Materials Research University, Pennsylvania State University, Oct. 2017.

Honors and Awards:

2018 Graduate Teaching Assistant Award.